TÉCNICO LISBOA

The effect of materials on the designs of open flue low NOx burner with non-cooled burner surface

Liliana Santos Matos

Thesis to obtain the Master of Science Degree in

Energy Engineering and Management

Supervisors: Prof. Fernanda Maria Ramos da Cruz Margarido
Prof. Edgar Caetano Fernandes

Examination Committee

Chairperson: Prof. José Alberto Caiado Falcão de Campos
Supervisor: Prof. Edgar Caetano Fernandes
Member of the Committee: Eng. Ricardo Marques Laranjeira

November 2017

Acknowledgments

To my supervisors, professor Edgar Fernandes and Fernanda Margarido, to all support, time and patience that they gave to my work. And to professor Teodoro Trindade to all support and help with some difficulties.

To my laboratory mates, Alexandre Ferro, Filipe Quintino, Francisco Mota, Gonçalo Serra, Ivo Monteiro, João Cunha, João Pires, João Toipa, José Rodrigues, Mariana Freire, Mário Pinto, Pedro Madeira, Pedro Santos, who helped me in many doubts with the thesis and even in moments outside the laboratory.

To Bosch Thermotechnology Aveiro to give me the tools I needed to develop my work. To all the people I worked with and who taught me so much.

To my parents who, unconditionally, supported me in every way and allowed me to get where I am and achieve all my dreams. To my brother for being a great support since always and for helping me in the smallest things. And to all my family for always believing in me and being a constant support.

To my dear friends, Andreia Duarte, Andreia Margarido, Luísa Ramalho, Joana Silva, Mariana Aurélio, Marta Palmeirim, Marta Reis, Raquel Frazão, Teresa Teles Branco, who believed in me since the first day I decided to change my life, who always supported me at all times and always celebrated my achievements with me. Far or near, whatever.

To you, Sérgio, my partner of all hours, for all that you have taught to me on this journey, for showing me, every day, the reasons why I am happy and for being an unconditional support.

Resumo

O controlo das emissões poluentes é um problema a nível mundial, o que explica porque motivo as indústrias emissoras têm direcionado a sua investigação no sentido da sua minimização. A indústria de soluções de aquecimento domésticas baseada em combustíveis de hidrocarbonetos está sob pressão por parte dos reguladores para limitar o nível de emissões perigosas, como NOx e CO. Há algumas soluções comercializadas que alcançam baixos níveis de emissões poluentes, mas é importante desenvolver soluções simples e economicamente viáveis que cumpram os limites impostos pela legislação.

Após análise dos materiais e modo de funcionamento de aparelhos domésticos de água quente, com foco em esquentadores atmosféricos que funcionam sob o mesmo princípio de bicos de Bunsen, usa-se o software Cambridge Engineering Selector para perceber os benefícios e limitações de cada material e o SimaPro para fazer uma avaliação de ciclo de vida para perceber qual o material com uma pegada ecológica mais baixa.

Usando diferentes materiais, obtém-se diferentes chamas e faz-se uma análise morfológica para saber como a variação do caudal de gás influencia as chamas de cada queimador, uma análise de espectroscopia para estimar a razão de equivalência e uma análise de termografia para saber as temperaturas do queimador.

Por fim, desenvolve-se um modelo matemático para prever a entrada de ar primário num queimador atmosférico de pré-mistura parcial.

Com os resultados obtidos, acredita-se que o ar primário não varia com o aumento da temperatura e que o efeito de impulsão se sobrepõe ao efeito do calor transferido no material.

Palavras-chave: Queimador atmosférico, Ar primário, Razão de equivalência, Emissões NOx

Abstract

There have been major concerns about pollutant emissions and this explains why the industries directly linked to these problems carry out their research in this direction. Domestic heating industry based on hydrocarbon fuels are under pressure from regulators to limit levels of harmful emissions such as NOx and CO. There are some commercialized solutions that reach low levels of polluting emissions, however it is important to develop simple and economically viable solutions that meet the limits imposed by legislation.

After analyzing the materials and working methods of domestic hot water appliances, focusing on atmospheric heaters that operate under the same principle as Bunsen burners, Cambridge Engineering Selector software is used to understand the benefits and limitations of each material and SimaPro to carry out a Life Cycle Assessment to understand which material has the lowest ecological footprint.

Using different materials, different flames are obtained and a morphological analysis is done to register how the variation of gas flow rate influence the flames for each Bunsen burner, then a spectroscopy analysis to estimate the equivalence ratio and a thermography analysis to find burner temperatures.

Finally, a simple 1D mathematical model is developed to predict air entrainment for a partially-premixed atmospheric burner.

With the results obtained, it is believed that the primary air does not change with the increase of temperature and that the buoyancy effect overlaps the effect of the heat transferred in the material.

Keywords: Self-aspirating burner, Primary air entrainment, Equivalence ratio, NOx emissions

Contents

Acknowledgments . . . iii
Resumo . . . v
Abstract . . . vii
List of Tables . . . xi
List of Figures . . . xiii
Nomenclature . . . xv

1 Introduction **1**
1.1 Motivation . . . 1
1.2 Objectives . . . 1
1.3 Thesis Outline . . . 2

2 Literature Review **5**
2.1 Materials and Properties . . . 8
2.1.1 Stainless Steel . . . 9
2.1.2 Brass . . . 9
2.1.3 Copper . . . 10
2.1.4 Aluminium . . . 11
2.1.5 Alumina . . . 11
2.1.6 Silicon Carbide . . . 12

3 Environmental assessment of materials **13**
3.1 Using Cambridge Engineering Selector . . . 13
3.2 Life Cycle Assessment . . . 16

4 Mathematical Model **21**
4.1 Burner geometry . . . 21

4.2 Assumptions and simplifications . . . 22
4.3 Modeling of primary air entrainment . . . 23
4.3.1 Burner model for primary air entrainment . . . 23
4.3.2 Flow from the injector to the mixing tube entrance . . . 24
4.3.3 Flow at the entrance of the mixing tube and mixing of air/fuel inside the mixing tube . . . 25
4.3.4 Flow through the flame region . . . 26

5 Experimental Setup **29**
5.1 Morphological Analysis . . . 29
5.2 Spectroscopy analysis . . . 30
5.3 Thermography analysis . . . 31
5.4 Uncertainty analysis . . . 33
5.4.1 Flow controllers uncertainty . . . 33
5.4.2 Chemiluminescense uncertainty . . . 33
5.4.3 Equivalence ratio uncertainty . . . 34
5.5 Porous burner surface . . . 34

6 Results and Discussion **35**
6.1 Morphological Analysis . . . 35
6.2 Spectroscopy analysis . . . 36
6.2.1 Spectroscopy I . . . 36
6.2.2 Spectroscopy II . . . 38
6.2.3 Spectroscopy III . . . 41
6.3 Thermography analysis . . . 42
6.4 Mathematical Model . . . 43

7 Conclusions **45**
7.1 Future Work . . . 46

Bibliography **47**

A Experimental results - Morphological analysis **51**

B Life Cycle Assessment results **55**

List of Tables

2.1 Stainless Steel properties. 9
2.2 Brass properties. 10
2.3 Copper properties. 10
2.4 Aluminium properties. 11
2.5 Alumina properties. 12
2.6 Silicon Carbide properties. 12

3.1 Life Cycle Assessment results. 18

5.1 Parameters for each tube tested. 30
5.2 Results for flow controllers uncertainty 33

List of Figures

2.1 Adiabatic flame temperature as a function of equivalence ratio for propane gas. 7

3.1 Thermal conductivity (W/(m.K)) for each material. 14
3.2 Melting point (°C) for each material. 14
3.3 Thermal expansion coefficient (μ strain/°C) for each material. 15
3.4 Maximum service temperature (°C) for each material. 15
3.5 Price (€/kg) for each material. 16
3.6 Comparision between each material on each impact category. 19

4.1 Bunsen burner geometry. 21
4.2 Typical values for headloss coefficient for different types of entrance. 25

5.1 Experimental setup Morphology analysis. 30
5.2 Flame observed in Tube 6 with gas flow rate of 0.5 SLPM. 31
5.3 Experimental setup Spectroscopy analysis. 32
5.4 Experimental setup Thermography analysis. 32
5.5 Porous burner surface used in all tests. 34

6.1 Flame observed in Tube 1 (a) and Tube 6 (b) with flow rate 0.5 SLPM. 36
6.2 Two different positions considered for the optical probe. 36
6.3 (a) Spectrum for tube 1 with the probe in position A (with a slit=0.50 mm) and (b) graph for the equivalence ratio. 37
6.4 (a) Spectrum for tube 1 with the probe in position B (with a slit=0.50 mm) and (b) graph for the equivalence ratio. 37
6.5 (a) Spectrum for tube 6 with the probe in position A (with a slit=0.50 mm) and (b) graph for the equivalence ratio. 38

6.6 (a) Spectrum for tube 6 with the probe in position B (with a slit=0.50 mm) and (b) graph for the equivalence ratio. 38
6.7 Optical probe at position (a) 1, (b) 2, (c) 3 and (d) 4. 39
6.8 (a) Spectrum for tube 6 with the probe in position 1 (with a slit=0.50 mm) and (b) graph for the equivalence ratio. 39
6.9 (a) Spectrum for tube 6 with the probe in position 2 (with a slit=0.50 mm) and (b) graph for the equivalence ratio. 40
6.10 (a) Spectrum for tube 6 with the probe in position 3 (with a slit=0.50 mm) and (b) graph for the equivalence ratio. 40
6.11 (a) Spectrum for tube 6 with the probe in position 4 (with a slit=0.50 mm) and (b) graph for the equivalence ratio. 40
6.12 Estimated equivalence ratio for the tube 6. 42
6.13 Spectrum for tube 6 at position 4. 42
6.14 Thermography results for a period of 300 s. 43
6.15 Relation between primary entrained air and equivalence ratio with tube diameter. 44
6.16 Relation between primary entrained air and tube diameter for different headloss coefficient (k_{12}). 44

A.1 Flames obtained for tube 1 with a gas flow rate from 0.10 to 0.60 SLPM. 51
A.2 Flames obtained for tube 2 with a gas flow rate from 0.15 to 0.60 SLPM. 52
A.3 Flames obtained for tube 3 with a gas flow rate from 0.15 to 0.60 SLPM. 52
A.4 Flames obtained for tube 4 with a gas flow rate from 0.25 to 0.60 SLPM. 52
A.5 Flames obtained for tube 5 with a gas flow rate from 0.25 to 0.60 SLPM. 53
A.6 Flames obtained for tube 6 with a gas flow rate from 0.10 to 0.60 SLPM. 53
A.7 Flames obtained for tube 7 with a gas flow rate from 0.10 to 0.60 SLPM. 53
A.8 Flames obtained for tube 8 with a gas flow rate from 0.15 to 0.60 SLPM. 54
A.9 Flames obtained for tube 9 with a gas flow rate from 0.15 to 0.60 SLPM. 54

B.1 Flow diagram for 0.119 kg of brass. Cut-off=10.9%. 56
B.2 Flow diagram for 0.041 kg of copper. Cut-off=10%. 57
B.3 Flow diagram for 0.052 kg of stainless steel. Cut-off=10%. 58
B.4 Flow diagram for 1.19E-04 kg of alumina. Cut-off=0.1%. 59
B.5 Flow diagram for 0.0447 kg of silicon carbide. Cut-off=4%. 60

Nomenclature

Greek symbols

ρ	Density [kg/m^3]

Roman symbols

Δh	Hydraulic headloss [m]
$\dot{m}$	Mass flow rate [kg/s]
A	Referring to area [m^2]
d	Referring to diameter [m]
g	Acceleration due to gravity [9.81 m/s^2]
k	Headloss coefficient
L	Length [m]
L_f	Flame length [m]
NOx	Generic term referring to the nitrogen oxides
p	Pascal [Pa]
R	Universal gas constant [$m^3.Pa.K^{-1}.mol^{-1}$]
T	Temperature [K]
U	Velocity [$\frac{m}{s}$]
V	Volume [m^3]
V_{23}	Flame volume [m^3]

Al_2O_3 Chemical symbol for Alumina

C_3H_8 Chemical symbol for Propane

CO_2 Chemical symbol for Carbon Dioxide

SiC Chemical symbol for Silicon Carbide

CES Cambridge Engineering Selector

Cu Abbreviation for Copper

LCA Life Cycle Assessment

LCI Life Cycle Inventory

SLPM Standart liter per minute

Stain.St. Abbreviation for Stainless Steel

Subscripts

air Referring to primary air entrainment

atm Referring to atmospheric/ ambient conditions

f Referring to gaseous fuel

inj Referring to injector

0 Referring to point (0) (injector's discharge orifice)

1 Referring to point (1) (mixing tube entrance)

2 Referring to point (2) (mixing tube exit/ bottom of the flame region))

3 Referring to point (3) (top of the flame region)

Chapter 1

Introduction

1.1 Motivation

Being an enthusiastic of renewable energies, learn more about conventional energy sources can be of great added value in today's times to find out the best way to use fossil fuels in order not to compromise future generations.

The sensitivity to this theme appeared when doing a Combustion course and with the aim of carrying out an internship at Bosch Thermotechnology in order to contribute to the development of new solutions in gas water heaters.

It is important to point out that through the last couple of years, with the growing of environmental concerns, global pollution warning has been increasing, leading to the development of new legislation that impose a significant reduction in pollutant emissions. Some innovation can be taken into account, trying to understand how the material used in a gas water heaters burner will influence the pollutant emissions.

1.2 Objectives

The main goal for this thesis is to analyse the materials and working methods of domestic hot water appliances, focusing on atmospheric heaters that operate under the same principle as Bunsen burners, understand the benefits and limitations of each material and carry out a Life Cycle Assessment to understand which material has the lowest ecological footprint. Then, using different materials with a specific geometry into some experimental tests and, finally, use that data to validate a mathematical model, that allows to predict the quantity of primary

air entrainment into the burner. Fulfilling these three goals, it is expected to accomplish the impacts of NOx and CO.

As it is possible to find in the work done by Namkhat and Jugjai [1], for the purposes of this thesis it is necessary to take into account experimental setup, burner geometry, different materials, injector geometry, the ambient conditions and fuel gas flow rate. The fuel gas type it is not important in this work, because it is only considered propane gas.

To meet these objectives, some tasks have to be considered:

- Define the materials that will be considered to the experimental part with only one setup to perform all the tests;
- Do morphological, spectroscopy and thermography analysis with the materials considered;
- Set all the assumptions and simplifications to be made when describing the physical phenomena occurring in the system to develop the equations for all points of interest of the burner and develop an algorithm to solve them as a function of the variable of interest (primary air entrainment);

1.3 Thesis Outline

This dissertation is organized in 7 main chapters, the Introduction which gives an overview of the work developed, talking about the motivation of this work, a general approach to the topic, also including the objectives to achieve.

Chapter 2 includes a literature review to contextualize the work done, including the main concepts and theoretical background, through the analysis of the materials most used today.

Chapter 3 develops two important analysis about the main properties of materials.

Chapter 4 is related to the mathematical model, burner geometry, assumptions and simplifications and all the equations of model.

In Chapter 5 it is presented the experimental setup of each analysis performed and an uncertainty analysis for each one.

The results are presented and discussed in chapter 6.

The conclusions of this work and recommendations for future work can be found in chapter 7.

Chapter 2

Literature Review

The topic of preventing pollutant emissions for the environment is not new, but in the last years, there has been a great concern about measures to avoid these emissions due to legislation that will be introduced in 2018.

As Costa and Coelho [2] stated in their book, this problem has received more attention from researchers, industries and governments, so it is therefore a natural commitment of the industrialized countries to legislate more restrictive limit values for NOx emissions.

They also list some control strategies that comply with the legislation, focusing on methods that have been developed to reduce NOx emissions. These methods may be divided in two groups:

- Modifications in the combustion process;
- Post-combustion methods.

In the first group, the main objective is to control physical phenomena that originate nitrogen oxides formation, so preventive solutions. In the second group, there are solutions to mitigate the consequences; those are measures to decrease the NOx emissions to the atmosphere formed in the combustion process.

The methods of the first group are namely the temperature control, recirculation of the combustion products, injection of water or water vapor, fuel staging, lean premixing and low NOx burners. The methods of the second group include selective non-catalytic and catalytic reduction.

Various types of combustion systems and burners have been studied due to the need of improving thermal performance and to reduce pollutant emissions, by developing the burner port geometry and the combustion system, as Hou et al. [3] and Jugjai and Rungsimuntuchart [4] did.

Talking about gas water heaters, it is possible to focus on the operation principle of a Bunsen burner, as it is most widely used. As Hou et al. [3] stated, this type is seen as a partially aerated burner where primary air entrains naturally carried out by the high velocity of the gas jet and ambient air, together. This primary air is mixed with the fuel gas before the occurrence of combustion.

A self-aspirating cold burner type do not drag the same quantity of air as a hot one. During combustion, the burner heats up, because the flame transfers heat to the tube; the same happens with air/fuel mixture as the fuel exits the injector to form the flame.

As stated by Namkhat and Jugjai [1] the study of preheating effect caused by combustion allows the investigation of a self-aspirating burner. It also allows to understand its operation mode and possible application to a heat recirculating combustion system for efficient energy. In order to achieve both improved thermal efficiency and reduced emissions of air pollutants, Zhen et al. [5] studied the effects of air preheat on the visual, thermal and emission characteristics in order to show that this technology of preheated air is one of the most useful and possibly implemented for domestic applications.

During this heating process, air/fuel mixture flow changes its properties (viscosity, density, velocity and others) and this leads to increased friction between the flow and the burner walls, so Reynolds number decreases, friction increases and the amount of entrained air decrease; this concept is usually called preheat effect. As it was written in the Patent No. 5 104 311 [6], the level of the primary air entrainment is of great importance for more complete combustion of the self-aspirating burners. Consequently, with the reduced air, NOx and CO emissions increase. For these reasons, there has been much research on this kind of burners.

Here it is important to explain in detail this preheat effect with the help of adiabatic flame

temperature plotted as a function of the fuel equivalence ratio (defined later in this document). It is possible to depict this plot in Figure 2.1, through a chemical kinetics simulation of the flame through the solver Cantera [7] using the GRI mech 3.0 reaction mechanism [8] to model the kinetics of the propane reactions as Salusbury and Bergthorson [9] did.

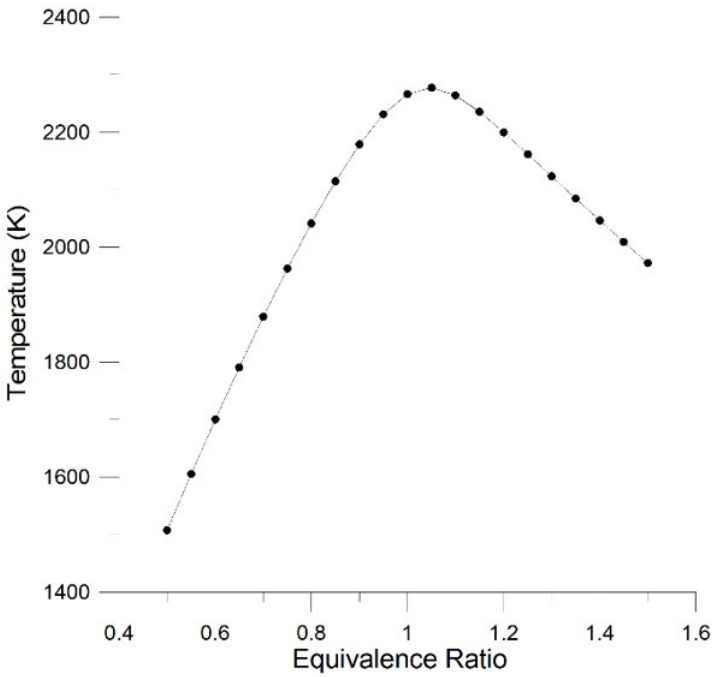

Figure 2.1: Adiabatic flame temperature as a function of equivalence ratio for propane gas.

So, depending on the type of flame, rich or lean, this preheat effect can have different consequences. If the flame is lean ($\phi < 1$), as the equivalence ratio increases, burner temperature increases, the amount of entrained air decreases, the flame and burner temperature increases even more and gets even less air, due to an increase in the flow resistance; this is called snowball effect.

If the flame is rich ($\phi > 1$), as the equivalence ratio increases, flame temperature decreases, having less impact in the entrained air. Then the snowball effect does not occur at this case and the buoyancy forces are likely to have more impact in this type of flames.

Looking at the work done by Namkhat and Jugjai [1], where the purpose was to get a good understanding about the effects of changes on the combustion air temperature on the primary aeration and flame structure, they found that the primary aeration decreased with an increasing preheated air temperature. They also proved that the preheating effect caused expansion of the

mixture and an increase in its viscosity. Finally, they recommended to take into consideration the preheating effect when designing the mixing tube and to obtain an accurate primary aeration.

Zhen et al. [5] experimentally investigated flames and they used a circular pipe burner to establish laminar Bunsen-type flame. They could relate NOx emissions with air preheated and found that NOx concentration increases as preheat temperature increases.

2.1 Materials and Properties

To proof the preheat effect already stated above, it is possible to use different materials in a Bunsen burner, as they may have different performances when applying to the burner, according to their properties.

In most products available on the market, the most commonly used materials are stainless steel, copper, steel, brass and aluminium. Due to the knowledge of their mechanical and physical properties these materials have been used for years as part of gas water heaters. Although aluminium has low melting point, it is widely used in these appliances, being constantly cooled through a system of water pipes.

So, when it comes to choose materials for a component, it is necessary to take into account many different factors. These factors can be, in general, material properties, material cost, availability, processing and environment [10]. In this work, focus will be given to material properties, material cost and environment.

Regarding material properties, there are some important ones to take into account when choosing materials to apply on this type of appliances, as thermal conductivity, temperature range, melting point, thermal expansion coefficient, density, high temperature resistance, among others.

To carry out some experimental tests, the materials mentioned above can be used and it is possible to study the hypothesis of using new materials.

2.1.1 Stainless Steel

Stainless steel is a steel alloy with chromium, nickel and often four or five other elements [11].

It is notable for its corrosion resistance, and it is widely used where both the properties of steel and corrosion resistance are required. It can be used in a range of applications because it is corrosion and staining resistant, requires low maintenance and has a long life cycle [12].

In addition to corrosion resistance, physical properties of stainless steel can include high and low temperature resistance, ease of fabrication, high strength and recyclable. Regarding temperature resistance, some stainless steel grades can retain high strength at very high temperatures. Relative to its high strength it can allow the use of thinner material, leading to lower weights and costs [13].

A good characteristic is that stainless steel is 100% recyclable. About 40% comes from end-of-life products [12].

Table 2.1: Stainless Steel properties.

General Properties	
Price (€/kg)	6.07–6.68
Density (kg/m^3)	7600-8100
Thermal Properties	
Melting point (°C)	1370-1450
Maximum service temperature (°C)	750-820
Thermal conductivity (W/(m.K))	12-24
Thermal expansion coefficient (μ strain/°C)	13-20

2.1.2 Brass

Brass is a metallic alloy made of copper and zinc. Adding zinc to the copper, allows observing some properties, making the brass a very versatile material. It is used for its strength and hardness, corrosion resistance (combined with formability and machinability), appearance, color and ease of working [14].

Zinc content increases the melting point and density, and thermal and electrical conductivity decrease. Also, the expansion coefficient, the strength and the hardness increase [15].

Brass is malleable and ductile, and can also be cast easily due to its low melting point [16].

Table 2.2: Brass properties.

General Properties	
Price (€/kg)	3.08–4.27
Density (kg/m^3)	7900-8550
Thermal Properties	
Melting point (°C)	882 – 967
Maximum service temperature (°C)	210
Thermal conductivity (W/(m.K))	100-130
Thermal expansion coefficient (μ strain/°C)	17-20.7

2.1.3 Copper

The challenge with copper is to design a material with the best combination of strength and conductivity [17].

Due to the fact of copper has a high electrical and/or thermal conductivity, it is widely used and it can be used in pure state or in alloys. Pure copper has excellent conductivity but poor strength. Moreover, the tensile properties strongly depend on the thermal-mechanical treatment and the impurity content [17].

In terms of mechanical properties, copper is malleable, which allow it to be shaped or bent, and ductile, easily pulled or stretched into a thin wire [18, 19]. Related to copper chemical properties it could corrode when exposed to air [19]. Finally, it also has the advantage of being recyclable.

Table 2.3: Copper properties.

General Properties	
Price (€/kg)	5.08–5.59
Density (kg/m^3)	8930-8940
Thermal Properties	
Melting point (°C)	982–1080
Maximum service temperature (°C)	180-350
Thermal conductivity (W/(m.K))	160-390
Thermal expansion coefficient (μ strain/°C)	16.9-18

2.1.4 Aluminium

Aluminium is considered the world's most abundant metal and is the third most common element comprising 8% of the earth's crust. Being very versatile makes it the most used material after the steel.

In the pure state, aluminum is soft, ductile, corrosion resistant, has a high electrical and thermal conductivity. Having low density, also has low weight, being one of the lightest engineering metals [20, 21].

It is also a material with high strength, superior malleability, easy machining and very easy to recycle.

Table 2.4: Aluminium properties.

General Properties	
Price (€/kg)	1.72-1.89
Density (kg/m^3)	2500-2900
Thermal Properties	
Melting point (°C)	475-677
Maximum service temperature (°C)	120-210
Thermal conductivity (W/(m.K))	76-235
Thermal expansion coefficient (μ strain/°C)	21-24

2.1.5 Alumina

Alumina (chemical symbol Al_2O_3) is considered an electrical and thermal insulator, but has a relatively high thermal conductivity for a ceramic material [22].

It is considered one of the most cost effective and widely used material in the family of engineering ceramics, due to its excellent combination of properties and an attractive price [22]. Alumina were identified as a temperature resistant material [23].

Among other key properties, alumina is a hard material and wear resistant, has good thermal conductivity for a ceramic material, high strength and stiffness. It is available as pure in a range from 94% to 99.8%, for the most demanding high temperature applications [22].

Table 2.5: Alumina properties.

General Properties	
Price (€/kg)	13.3–20.1
Density (kg/m^3)	3800-3980
Thermal Properties	
Melting point (°C)	2000-2100
Maximum service temperature (°C)	1080-3700
Thermal conductivity (W/(m.K))	26-38.5
Thermal expansion coefficient (μ strain/°C)	7–7.9

2.1.6 Silicon Carbide

Silicon Carbide (chemical symbol SiC) is a high quality ceramic with very good mechanical properties. It has applications in resistance heating, flame igniters and electronic components. As its main properties, it has low density, high mechanical strength, low thermal expansion, high thermal conductivity, high hardness and excellent thermal shock resistance [23]. The combination of high thermal conductivity with low thermal expansion and high strength, gives this material exceptional thermal shock resistant qualities [24]. It has the highest corrosion resistance of all advanced ceramics. Disadvantages may be the fact that it is brittle and the recycling process is very complex [15].

Table 2.6: Silicon Carbide properties.

General Properties	
Price (€/kg)	10.6 – 15.2
Density (kg/m^3)	3100-3210
Thermal Properties	
Melting point (°C)	2150-2500
Maximum service temperature (°C)	1400-1700
Thermal conductivity (W/(m.K))	80-130
Thermal expansion coefficient (μ strain/°C)	4–4.8

Chapter 3

Environmental assessment of materials

In order to present a detailed study on each mentioned material and focusing on the properties referred in previous section, two important analysis will be developed in order to find the materials that better fit the purpose of this work.

3.1 Using Cambridge Engineering Selector

In order to compare the materials stated above, regarding some properties already mentioned and in order to indicate what could be the material that better fit the purpose of this work, Cambridge Engineering Selector (CES) software was used, allowing the combination of engineering, economic and environmental properties [25].

With this software, it is possible to choose the materials to be compared according to some properties, make comparative graphs and analyze the relationships between the properties of each material. Materials properties charts are a great way to visualize and communicate materials properties [25].

Starting to focus on some important properties, some figures will be presented regarding each property for a range of materials.

Regarding thermal conductivity, checking Figure 3.1, it is possible to see that copper has the highest thermal conductivity and stainless steel the lowest.

Regarding the melting point, silicon carbide has the highest melting point and aluminum

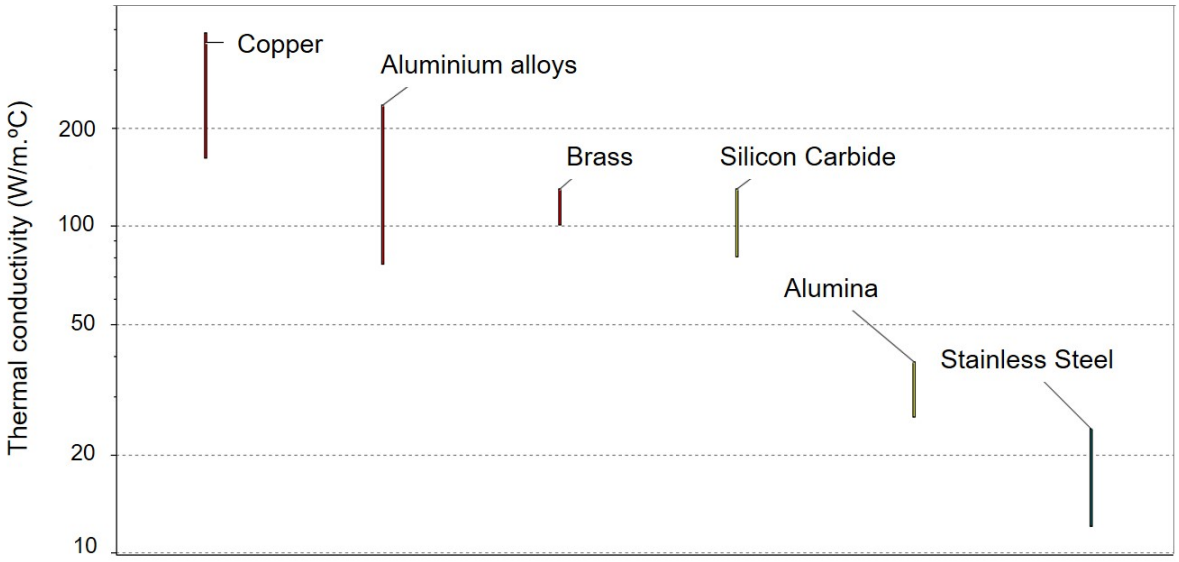

Figure 3.1: Thermal conductivity (W/(m.K)) for each material.

alloys have the lowest, as observed in the Figure 3.2.

This property is very important, because it is related with the characteristic flame temperature, formed by the combustion of LPG with air. Considering stoichiometry, adiabatic flame temperature for propane is 1970 °C (2243K - 2300K) [2].

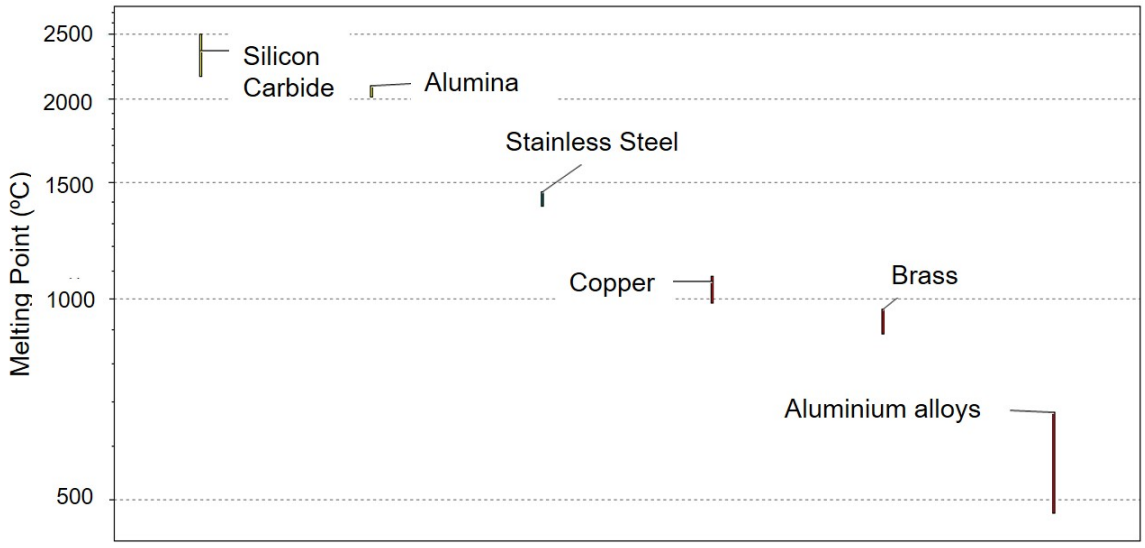

Figure 3.2: Melting point (°C) for each material.

Talking about thermal expansion coefficient (Figure 3.3), silicon carbide has the lowest value and brass has the highest. This property may be important to ensure that the material does not change its shape when it reaches higher temperatures.

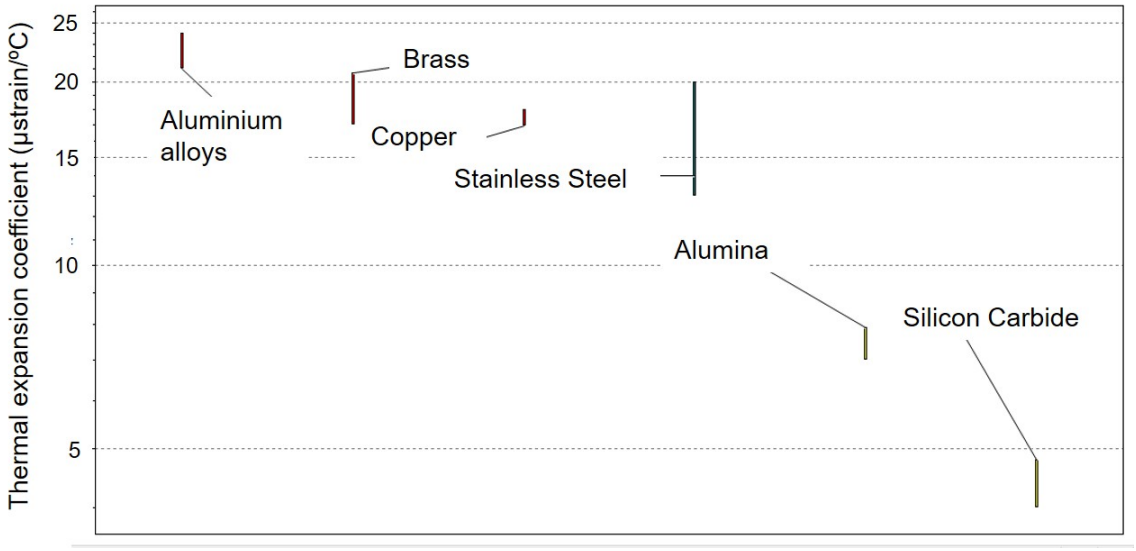

Figure 3.3: Thermal expansion coefficient (μ strain/°C) for each material.

Now, checking Figure 3.4 that presents the maximum service temperature, it is possible to see that, although silicon carbide has a small range of temperatures, it has the highest maximum service temperature, while aluminum alloys have the lowest.

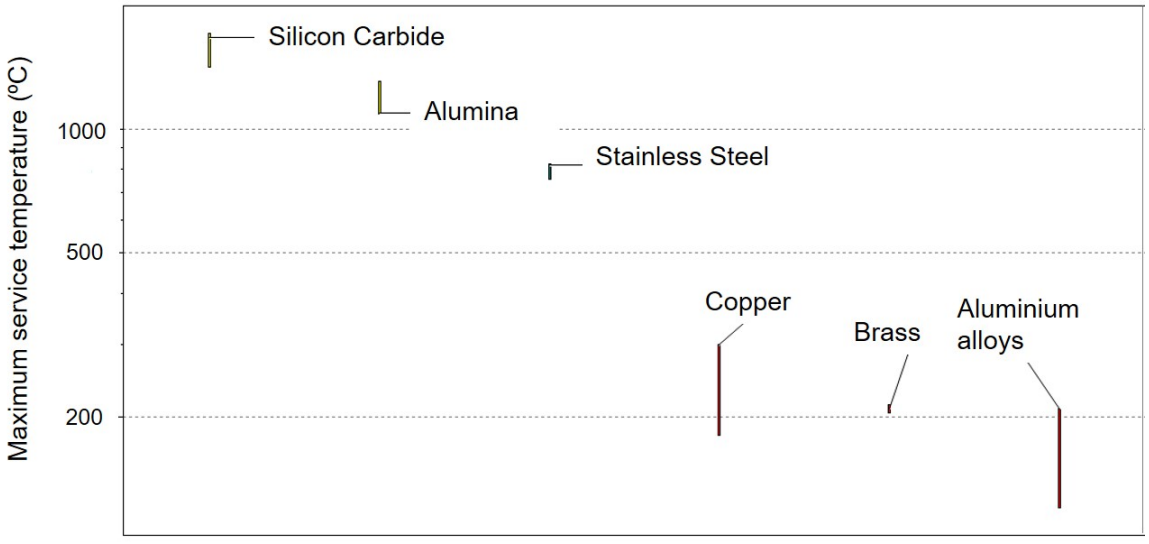

Figure 3.4: Maximum service temperature (°C) for each material.

Finally, regarding the price (Figure 3.5), although it may not be up to date, it is clear that alumina is the most expensive material and aluminium alloys are the cheapest materials.

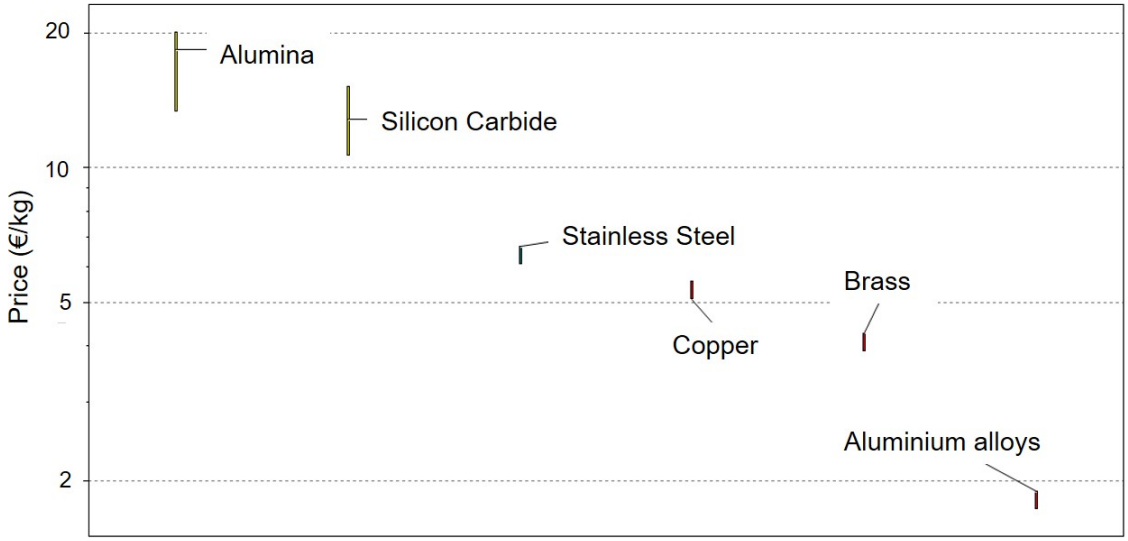

Figure 3.5: Price (€/kg) for each material.

Even knowing that only these characteristics are not enough to determine the material to use, it is possible to conclude that, probably, silicon carbide is the material that better fits to the purpose of this work. Despite the high price, it has a good thermal conductivity, the highest melting point, the lowest thermal expansion coefficient, the maximum service temperature and a medium price comparing to the other materials.

3.2 Life Cycle Assessment

In order to complement the analysis done with CES software, with a Life Cycle Assessment it will be possible to add another analysis feature and thus improve the conclusion on the material(s) to use.

Life Cycle Assessment (LCA) is used as a tool to assess the environmental impacts of a material, product, process or activity throughout its life cycle. This analysis starts with the extraction of raw materials through to processing, transport, use and disposal, being in this case known as cradle-to-grave [26].

Because it is the most common internationally accepted and acknowledged tool for assessing and demonstrating the environmental behavior of systems [27], it has many applications to governments, to industries, to services and to the consumer, focusing on its environmental behavior, process improvement and product design. It is also used as the basis of eco-labelling [26]. The main disadvantage of this tool is the need for high quality data to ensure reliable

results [27].

Bovea et al. [27] had chosen to perform a cradle-to-gate analysis, which considers only the processes within the factory, and there is another approach that consider all processes till the end of life of the material, named cradle-to-grave. But the most correct analysis to do is a cradle-to-cradle, which considers the recycling process and reuse of the material, representing the principle of circular economy [28], being restorative and regenerative and based on three principles: preserve and enhance natural capital, optimise resource yields and foster system effectiveness.

A life cycle assessment consists of four steps, according to ISO 14040-44 [29]:

Goals and scope: The purpose of this study was to perform an environmental assessment of different materials already described in previous sections, with the aim to identify which of these materials had a greater impact on the environment. When doing such an analysis, it is necessary to define a functional unit, which was defined as 1 kg. The aim of this study was to perform a cradle-to-gate environmental assessment, considering that the material was received ready to use, without the need for any additional process, being the manufacturer responsible for the recycling and recovery process.

Life Cycle Inventory: To perform inventory analysis, the data was compiled directly from the SimaPro database, considering all relevant energies, materials, emissions and wastes [30]. The main output that will coming out from this LCI will be a flow diagram that will define the inputs and outputs in the system. The accuracy of the results and the time and resources required are assessed by the complexity of the diagram, the more complex the diagram, the more accurate the results and more time and resources will be needed. These diagrams will be placed in Appendix B. In this step it was necessary to select the timeframe. Here the choice is subjective and it was decided to select an egalitarian perspective, considering a 500 year timeframe, being a long term perspective it provides a further vision to the future and it is the most precautionary perspective [31].

Impact Assessment: SimaPro is a decision support tool with the objective of monitor and measure the environmental impacts of each material [32]. For this reason, some impact categories were considered (Climate change, ozone deletion, marine eutrophication, human toxicity,

metal depletion, fossil depletion and others). Each sample used in the experimental tests was previously weighed to carry out this analysis. Bar graphs will be obtained representing the results by impact category and they will be placed all-in-one further down in this section, allowing a comparison between all materials studied. The method to apply a Life Cycle Assessment is midpoint-oriented, that convert the emissions of hazardous substances and extractions of natural resources into impact category indicators at the midpoint level [31].

Interpretation: In this last step will be evaluated some opportunities to reduce energy, material consumption or environmental impacts at each stage of the product life-cycle. From this analysis, a value of kg CO_2 equivalent is immediately obtained for each material. This means that for the quantity of material needed, x kg CO_2 equivalent was emitted to the atmosphere. These resulting units are often presented, but they are difficult to understand. For those reasons, it is necessary to normalize them in way to interpret the resulting values easier. This normalization consists of dividing the obtained values by a reference situation' scores, considering the number of citizens in Europe [33]

Taking into account the quantities of material required for the manufacture of tubes 8 cm high and diameters varying between 1.1 and 2 cm, the results obtained are shown in Table 3.1.

Table 3.1: Life Cycle Assessment results.

#	Material	Diameter (cm)	Mass (kg)	kg CO_2 eq.
1	Brass	2	0.119	6.18E-5
2	Copper	2	0.041	2.1E-5
3	Stainless Steel	1.1	0.052	2.23E-5
4	Alumina	2	0.054	1.19E-4
5	Silicon Carbide	2	0.0447	3.3E-5

Tubes made of brass, copper and stainless steel were used in experimental tests performed according to the purpose of this work. The other two tubes were considered as having the same length as the previous ones and with a diameter equal to the majority, taking into account the density of each material.

When focusing on climate change, brass and silicon carbide presents the highest value of

kg CO_2 eq. (Table 3.1), taking into account that, probably, using a stainless steel tube with the same diameter as the others, the result could rise to a value close to silicon carbide.

Looking at the bar graph that results from Simapro (Figure 3.6), it is possible to see the impact categories with the highest values for each analyzed material.

It is possible to conclude that, comparing with the other impact categories, climate change, marine eutrophication, particulate matter and terrestrial ecotoxicity are the ones that presents the lowest values.

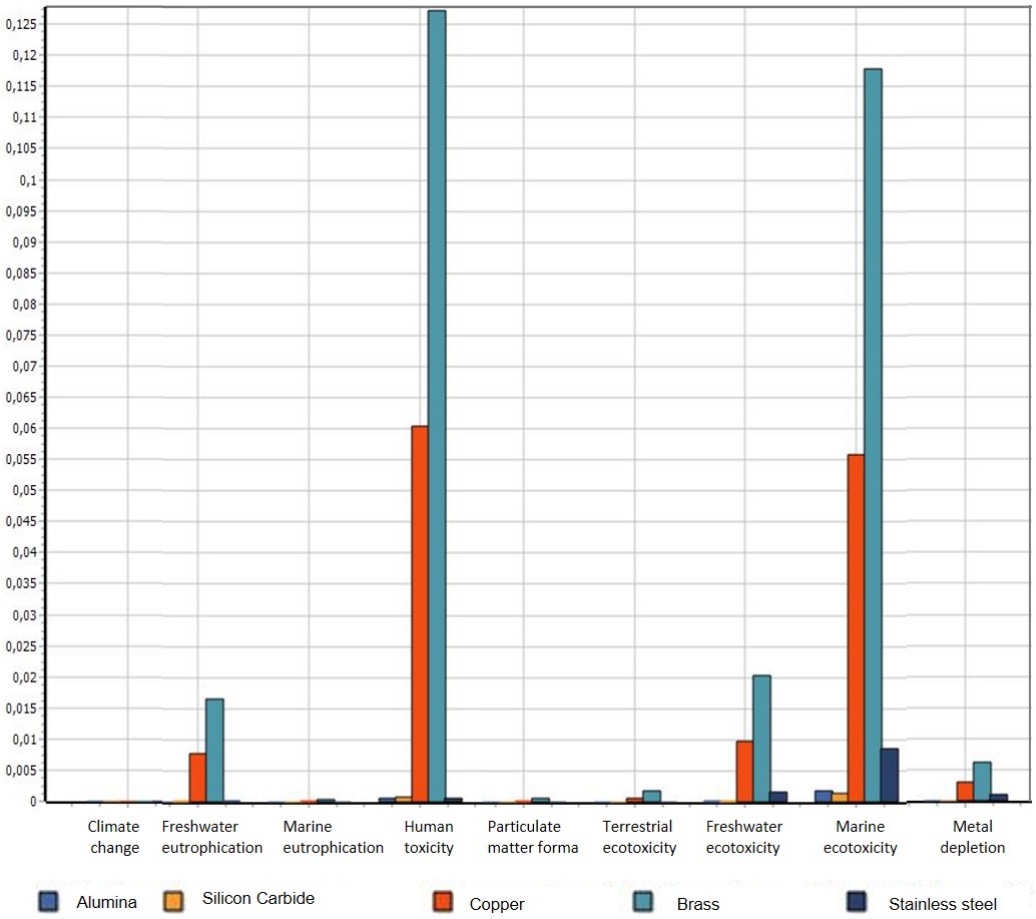

Figure 3.6: Comparision between each material on each impact category.

Freshwater eutrophication is seen as a form of inland water pollution and it is caused by nutrient enrichment of the aquatic environment as a result of human activities [31]. It can be helpful to understand the ecological quality of water [31] and it is possible to conclude from the graph that copper and brass have the highest values for this category.

Human toxicity and marine ecotoxicity are the impact categories with the highest values found in this analysis, with greater contribution by brass and copper. These categories take into

account environmental persistence, accumulation in the human food chain and the toxicity of a chemical [31]. Despite having lower values, freshwater ecotoxicity is also caused by the factors listed above.

Metal depletion is related with large-scale exploitation of minerals and metals to produce materials for the purpose intended by man and it is possible to verify that there is some impact by the exploitation of brass, copper and stainless steel.

It is clearly visible from the graph that brass and copper are the materials with the most impact in this analysis, which is probably related to the inputs observed in flow diagrams for brass and copper, as it is possible to see in Appendix B.

It follows from these two analysis that it is complicated to have a material which combines all the characteristics.

Chapter 4

Mathematical Model

4.1 Burner geometry

Presented in Figure 4.1 is the Bunsen burner type with all the elements considered in this work. It is important to note that in this work some constituents of a gas water heater were not considered, such as the combustion chamber and the heat exchanger. So it were considered:

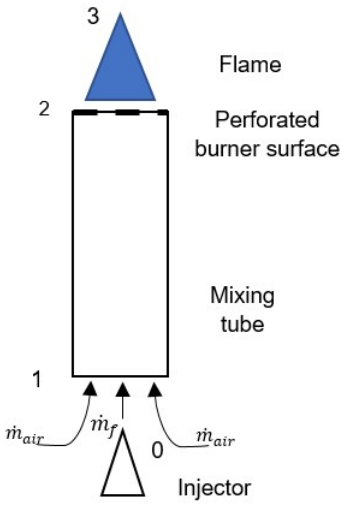

Figure 4.1: Bunsen burner geometry.

- Injector, which discharges a mass flow $\dot{m}_f$ of propane gas C_3H_8 through the entrance of the mixing tube (1);
- (1 to 2) Mixing tube with a circular cross section, with a specific diameter d, where a

mass flow of entrained air $\dot{m}_{air}$ mixes with the fuel, originating a homogeneous mixture in the end of the tube (2);

- (2) Perforated burner surface where the flame is anchored;
- (3) Partially premixed flame where the air/fuel mixture is burned.

For the purpose of this work, the entrainment of a secondary mass flow of ambient air is not considered.

It is important to use a porous burner surface, as Keramiotis et al. [34] stated, because porous burners are characterized by low pollutant emissions, enhanced combustion stability across a wide range of conditions and the potential to operate in ultra-lean combustion regimes.

4.2 Assumptions and simplifications

The objective of the model was to predict the quantity of primary air entrainment into the burner. In order to achieve this objective, it was necessary to take into account the burner geometry, the ambient conditions and the gas flow.

The assumptions considered for the model were:

1. Steady-state regime;
2. The propane gas obeys the perfect gas law;
3. The mixing tube is long enough in order to allow a perfect mixing between the fuel and the air;
4. The flow is considered to be one-dimensional, means that the properties only change along the longitudinal direction;
5. Changes in potential and kinetic energies are ignored;
6. Combustion is complete.

4.3 Modeling of primary air entrainment

In this section it will be developed some analytic expressions for the pressures of the burner from position (0) to position (3). Some parameters should be considered when deriving the expressions for pressures at all these points:

- Internal geometry of the injector, considering the discharge coefficient that is dependent on the shape of the injector orifice and on the Reynolds number for flow through the orifice. It is important to consider this coefficient as the gas flow is less than expected, because of the frictional losses and the vena-contracta effect;
- Internal geometry of the burner, considering section area and lengths;
- Headloss coefficient related with primary air entrainment into the mixing tube, thus dependent on burner geometry (type of entrance) and flow characteristics;
- Ambient conditions (pressure, temperature and density);
- Fuel characteristics (heating value, density, composition, etc) and gas flow rate;
- Flame geometry, considering the height and the section area;
- Primary air entrainment $\dot{m}_{air}$ which is the variable to be calculated using the model as a function of the parameters listed above.

All the parameters listed above must be input by the user of the model, except the last one.

To obtain the expressions of p_1 and p_2 it is necessary to resort to an iterative process, because in these points there is dependence of $\dot{m}_{air}$.

4.3.1 Burner model for primary air entrainment

In the model developed in this section, it was considered that the injector is discharging a certain mass flow rate of fuel $\dot{m}_f$ into the burner. Here, the ignition of the mixture occurs and buoyancy effects $gV(\rho_{atm} - \rho)$ are considered between points (2) and (3), where V is the flame volume.

In all sections of the model, the density of the mixture is given by:

$$\rho = \frac{p}{RT} \tag{4.1}$$

where the values for R and pressure p are constant at all points. Temperature T vary in each one of the points.

For this purpose, it is important to start by defining the equation for the equivalence ratio which is a function of the air and gas flow rate.

$$\Phi = \frac{\frac{m_a}{m_f}}{(\frac{m_a}{m_f})_{est}} \tag{4.2}$$

4.3.2 Flow from the injector to the mixing tube entrance

In this first part of the stream considered, from the injector (0) through mixing tube entrance (1), the mass flow rate of fuel $\dot{m}_f$ is known and a mass of air from ambient air around the tube enters into the mixing tube in (1) – primary air. At that time, this mass flow rate $\dot{m}_{air}$=$\dot{m}_0$ is unknown and the model will be useful to compute this primary air stream.

The fuel mass flow exits the injector, with a circular section, a diameter d_{inj} and the primary air enters the burner through the inlet of the mixing tube with a cross-sectional area of A_1, at a pressure p_1 equals to the ambient pressure. Temperature T_1 is considered, being the temperature registered at that point.

It was considered that the air flow is constant, adiabatic and incompressible, from the surrounding atmosphere to the point (1) and thus the generalized form of the Bernoulli's equation can be applied between points (0) and (1), considering, only, the existence of an air flow.

$$p_1 - p_0 = \frac{1}{2}\rho_0(\frac{\dot{m}_0}{\rho_0 A_1})^2 - \rho_0 g \Delta h_{01} \tag{4.3}$$

where $\frac{\dot{m}}{\rho A}$ is the velocity of the flow and ρ is the density of the flow. In point (0) the atmospheric conditions were verified, then $p_0 = p_{atm}$.

The term Δh_{01} is the headloss experienced by the primary air entering into the mixing tube and it is given by:

$$\Delta h_{01} = \frac{k_{01}}{2g}(\frac{\dot{m}_0}{\rho_0 A_1})^2 \tag{4.4}$$

Here the k_{01} appears, representing the headloss coefficient that is highly dependent on the type of entrance considered. Typical values for this coefficient for different types of entrance are presented in Figure 4.2 (original from Çengel and Cimbala [35]). Is was assumed 0.5 as an input to the model.

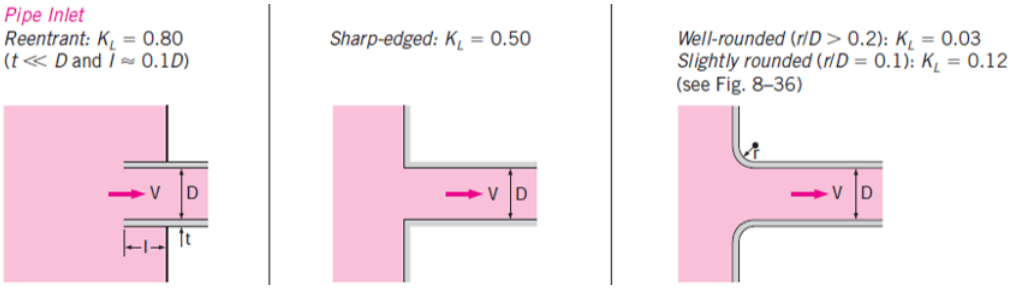

Figure 4.2: Typical values for headloss coefficient for different types of entrance.

4.3.3 Flow at the entrance of the mixing tube and mixing of air/fuel inside the mixing tube

In this second part it was verified the entry of the mixture into the tube (1) and its propagation up to the point (2). Here, the same conditions were considered.

The mixture that entrains in the mixing tube represents the mixture of the fuel with the primary air, so $\dot{m}_1 = \dot{m}_0 + \dot{m}_f$, being $\dot{m}_0 = \dot{m}_{air}$. The mixture enters at the tube, which has a cross-sectional area of A_1, and starts to propagate over a distance L, till the end of the tube in point (2) which also has a circular section with a cross-sectional area A_2 and it's considered that A_1=A_2. The density of the mixture is given by:

$$\rho_m = \frac{(\dot{m}_f + \dot{m}_0)}{(\frac{\dot{m}_f}{\rho_f}) + (\frac{\dot{m}_0}{\rho_0})} \tag{4.5}$$

Resultant equation is given by:

$$p_2 - p_1 = \frac{1}{2}\rho_1(\frac{\dot{m}_1}{\rho_1 A_1})^2 - \frac{1}{2}\rho_2(\frac{\dot{m}_2}{\rho_2 A_2})^2 - \rho_2 g \Delta h_{12} \tag{4.6}$$

where, at this point, ρ_1 and ρ_2 are the density of the misture ρ_m.

In this step it is considered that the mass flow rate that entrains at the mixing tube is the same that reach the end of this tube, so $\dot{m}_2$=$\dot{m}_1$. Temperature T_1 is considered again and T_2 the temperature observed at the end of the tube. The term Δh_{12} is the headloss experienced by the mixture flowing into the mixing tube:

$$\Delta h_{12} = \frac{k_{12}}{2g}(\frac{\dot{m}_1}{\rho_1 A_1})^2 \tag{4.7}$$

Here the k_{12} appears, representing the headloss coefficient that is dependent on the friction losses in the tube, related to the length L and roughness. Is was assumed 0.02 as an input to the model.

4.3.4 Flow through the flame region

In the flame region, combustion occurs and the flow changes its temperature, pressure, velocity, density and composition. The temperature at which combustion reaction occurs is admitted to be constant across the flame region. Temperature T_3 is the flame temperature.

In this region it is important to introduce the momentum equation, considering it between points (2) and (3):

$$p_2 A_2 - p_3 A_3 + g V_{23}(\rho_{atm} - \rho_{23}) = \rho_3 A_3 U_3^2 - \rho_2 A_2 U_2^2 \tag{4.8}$$

where V_{23} is the volume occupied by the flame, considering a parallelepiped whose base area A_3 is the section area of the tube ($A_3 = A_2$) and the height L_f is the height of the flame, so $V_{23} = A_3 L_f = A_2 L_f$. In this step it is considered that $\rho_{23} = \rho_3$ and that the mass flow rate coming out of the tube is the same as reaching the top of the flame, so $\dot{m}_3 = \dot{m}_2$.

Through the mass balance equation, it is possible to conclude that

$$\rho_3 A_3 U_3 - \rho_2 A_2 U_2 = 0 \tag{4.9}$$

Considering $A_3 = A_2$, 4.9 can be simplified to $U_3 = \frac{\rho_2}{\rho_3} U_2$. Substituting in Equation 4.8, one gets $A_2(P_2 - P_3) + g V_{23}(\rho_{atm} - \rho_3) = \rho_2 A_2 U_2^2 (\frac{\rho_2}{\rho 3} - 1)$, which results in the following equation:

$$p_3 - p_2 = -\frac{\rho_2 A_2 U_2^2 (\frac{\rho_2}{\rho_3} - 1) - g V_{23} (\rho_{atm} - \rho 3)}{A_2} \tag{4.10}$$

In the end:

$$\begin{aligned} & p_0 + \frac{1}{2} \frac{\dot{m_0}^2}{\rho_{atm} A_1^2} (1 - k_{01}) = \\ & = \frac{\rho_m A_2 (\frac{m_0 + m_f}{\rho_m A_1})^2 (\frac{\rho_m}{\rho_3} - 1) - g V_{23} (\rho_{atm} - \rho_3)}{A_2} + p_0 + \frac{1}{2} \frac{(\dot{m_0} + \dot{m_f})^2}{\rho_m A_1^2} (-1 - 1 - k_{12}) \end{aligned} \tag{4.11}$$

Chapter 5

Experimental Setup

To complement the mathematical model derived in previous section it was necessary to perform some experiments in a simple prototype, Bunsen burner type. Three different tests were performed; a morphological analysis to specify the flame behavior for each tube, since the only variable manipulated by the user was the gas flow rate; a spectroscopy analysis to estimate the equivalence ratio of the flames considered; and a thermography analysis to find the temperatures at the entrance of the tube (1) and at the exit, where flame was anchored (2).

All these tests were performed with flame anchored at the end of the tube, thus were controlled by Lab View software (Alicate Scientific MC-1SLPM-D/5M for propane) to input a gas flow rate.

As already mentioned in the previous section, a perforated burner surface or quenching net was used, primarily to avoid flashback (i.e. to prevent the flame propagation towards the source of gas), but also to reduce pollutant emissions.

5.1 Morphological Analysis

In this first analysis, different tests were performed, and the objective was to understand the behavior of the flames by varying some key elements, as mixing tube internal and external diameter, consequently the surface area, and the tube material, keeping always the same height.

Table 5.1 portrayed the parameters mentioned and summarized.

The gas flow rate in this test was varied between 0.1 and 0.6 standard liters per minute (SLPM), resulting in different flames for each tube and each flow. The photographic record of these flames was carried out with a Canon 500D.

Table 5.1: Parameters for each tube tested.

Tube number	1	2	3	4	5	6	7	8	9
dint (cm)	1.1	2.1	2.24	1.7	2.1	2.0	1.9	1.9	2.0
dext (cm)	1.5	2.2	2.5	2.5	2.5	2.5	2.5	2.5	2.2
Thickness (cm)	0.2	0.05	0.13	0.4	0.2	0.25	0.3	0.3	0.1
Height (cm)	8.0	8.0	8.0	8.0	8.0	8.0	8.0	8.0	8.0
Surf. area (cm^2)	0.817	0.338	0.968	2.639	1.445	1.767	2.074	1.956	0.660
Material	Stain.St.	Stain.St.	Stain.St.	Brass	Brass	Brass	Brass	Brass	Cu

Although the only input was gas, which enters the pipe through the injector, it was also considered a primary air entrainment that mixes with the gas along the pipe to form the flame at perforated surface.

Figure 5.1 shows the experimental setup used to perform these tests.

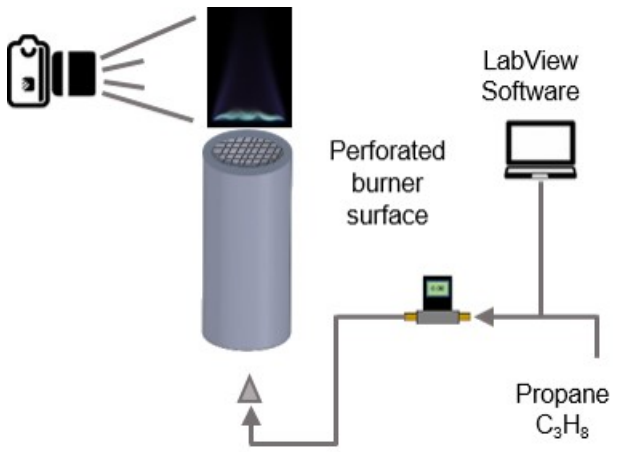

Figure 5.1: Experimental setup Morphology analysis.

5.2 Spectroscopy analysis

In order to estimate the equivalence ratio of the flames considered in the previous analysis, a detailed analysis of the flame was performed using spectroscopy.

This analysis had a great contribution to the primary air entrainment computation, since the objective here was to estimate the equivalence ratio and, knowing the gas flow rate, easily the primary air entrainment is obtained. It is based on the chemiluminescence emission of the flame by recording the spectrum of flame emission between 250 and 575 nm by means of an Optics HR2000 High-resolution Miniature Fiber Optic Spectrometer.

In this method, an optical fiber was used at the flame in study and it was placed in such a way that their field of view contained a reduced flame volume using a slit opened by 0.20, 0.25, 0.50 and 0.75 mm, to ensure that the contribution of the flame was only from that fiber bundle.

A flame like the one in Figure 5.2 emits radiation mostly due to OH^*, CH^* and C_2^* radicals, approximately at 310, 430 and 515 nm, respectively. They appear in the course of reactions that occur during the combustion process, such as formation and dissociation reactions, and they are important points to compute the equivalence ratio. Figure 5.3 shows the experimental setup used to perform these tests.

Figure 5.2: Flame observed in Tube 6 with gas flow rate of 0.5 SLPM.

5.3 Thermography analysis

As an input to the mathematical model, it was necessary to find the temperatures verified at the tube entrance (1) and at the end (2), where the flame was anchored.

In this test, temperatures were recorded using an infrared camera, an Onca-MWIR-InSb from Xenics that gives ”images” of the temperature field of the object under study, having the ability to read the infrared radiation with its sensors. The result will be a two-dimensional temperature field with an accuracy of +/- 0.5°C. A camera software was used to record and process the data collected, according to the experimental setup shown in Figure 5.4.

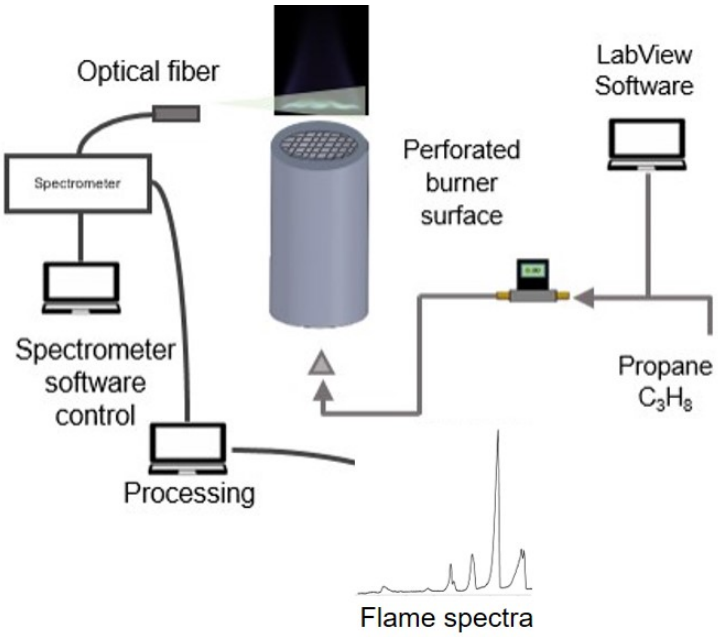

Figure 5.3: Experimental setup Spectroscopy analysis.

With a camera pointed at the object, it was necessary to make a calibration for the desired distance with a black object. After this calibration, keeping the camera in the same position, it was possible to collect the temperature data.

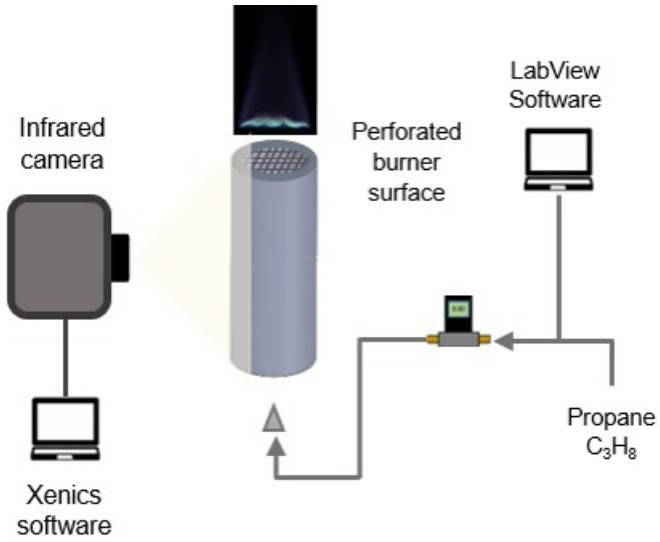

Figure 5.4: Experimental setup Thermography analysis.

5.4 Uncertainty analysis

In this section, focus will be given to the calculation of the uncertainties associated with the experiments carried out in this work. The uncertainty of the equivalence ratio and chemiluminescence results obtained is a consequence of the flow controllers, the spectrometer measurements and the data treatment.

5.4.1 Flow controllers uncertainty

The flow controller used in the experimental tests has an associated uncertainty: 0.8% of the flow measured over 0.2% of its full scale. This can be put in the following equation, where the total uncertainty can be computed for a certain flow rate in a flow controller:

$$U_Q = \pm(0.008Q_m + 0.002Q^i_{max}) \tag{5.1}$$

where U_Q is the uncertainty of flow rate Q, Q_m is the flow rate that were measured and Q^i_{max} is the maximum operating flow rate of flow controller i, so the error associated with each flow rate depends not only on the measured flow rate, but also on the maximum operating value of the flow controller. Using flow controller with the lowest maximum operating value possible allows decreasing the uncertainty of the experimental flow rate and the associated error (e_Q).

Table 5.2: Results for flow controllers uncertainty

Gas	Highest Q_m (SPLM)	Q^i_{max} (SPLM)	U_Q	e_Q (%)
C_3H_8	0.6	1	0.0068	1.13

5.4.2 Chemiluminescense uncertainty

The fiber optic spectrometer used in the experimental tests has an associated uncertainty related with the OH^*/CH^*, CH^*/C_2^* and C_2^*/OH^* ratios.

From the spectrum file the objective was to find the maximum value for each radical, taking into account the range of wavelengths where each one emits, and easily the value of the ratios were reached.

The next step was to calculate the uncertainty of each radical (U_{OH*}, U_{CH*} and $U_{C_2^*}$) and, finally, the uncertainty for each ratio (being A and B different radicals):

$$U_{\frac{A}{B}} = \sqrt{(\frac{1}{B})^2 \times U_A^2 + (\frac{A}{B^2})^2 \times U_B^2} \tag{5.2}$$

To calculate the relative error, proceeded as follows:

$$e_{\frac{A}{B}} = \frac{U_{\frac{A}{B}}}{\frac{A}{B}} \tag{5.3}$$

5.4.3 Equivalence ratio uncertainty

For this analysis a reference flame from a Bunsen burner with propane-air mixture were considered and a calibration equation was obtained for each OH^*/CH^*, CH^*/C_2^* and C_2^*/OH^* ratios, corresponding to equivalence ratio, which has an associated uncertainty.

Using the calibration curve for each ratio, an experimental value for equivalence ratio was obtained. The maximum deviation between each experimental value and the predicted value was determined, being the maximum error value: $e_\phi = 7\%$.

5.5 Porous burner surface

Porous surface used is shown in Figure 5.5, it has been sized to the internal diameter of each tube and has a mesh having an area of 0.074 x 0.074 cm^2.

Figure 5.5: Porous burner surface used in all tests.

Chapter 6

Results and Discussion

In this chapter, the results of the experimental tests performed in the Bunsen burner will be presented for the different types of analysis performed.

6.1 Morphological Analysis

As stated in previous section, morphological analysis was important to know the different types of flames that resulted from the use of different tubes varying some key elements such as mixing tube internal and external diameter and the tube material, keeping always the same height. From a large set of flames, two distinct flames were verified; one with a yellow tip and one with a flame with small oscillations near the perforated burner surface and a plume.

Referring to Table 5.1, where the tubes are numbered from 1 to 9, the numbering attributed to each tube was useful for presenting the results. Figure 6.1 presents the flames for tubes 1 and 6, with a gas flow rate of 0.5 SLPM. All the flames obtained in this test can be seen in Appendix A.

With this analysis, it was decided to choose two different tubes to make the next proposed analysis. As the flames are quite similar from the tube 2 till 9, tubes 1 and 6 were chosen to perform spectroscopy and thermography analysis.

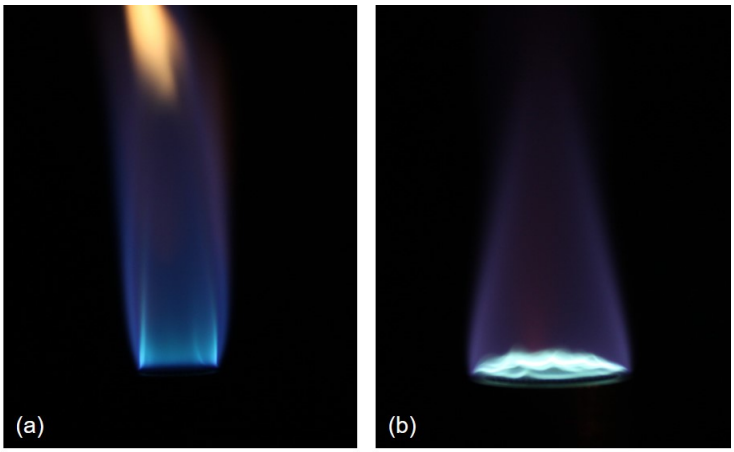

Figure 6.1: Flame observed in Tube 1 (a) and Tube 6 (b) with flow rate 0.5 SLPM.

6.2 Spectroscopy analysis

In order to estimate the equivalence ratio of the flames considered in the previous analysis, it was decided to perform a spectroscopy analysis of the flames.

To facilitate the analysis of these results, the spectroscopy study was divided into three different tests, representing three different approaches.

All spectra presented in these subsections represent an average of the spectra collected per second, during 50 seconds.

6.2.1 Spectroscopy I

In this first approach, tubes 1 and 6 were tested considering two different positions (A and B) for the optical probe for each tube, as it is possible to see in Figure 6.2, and a data collection time of 50 s.

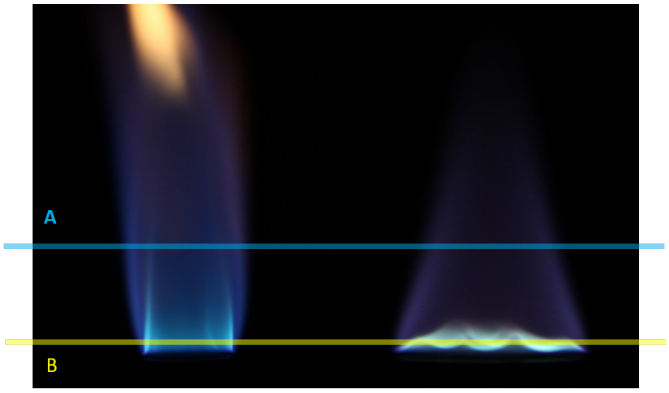

Figure 6.2: Two different positions considered for the optical probe.

In tube 1, the analysis was performed for two different gas flows rates, 0.25 and 0.50 SLPM.

It was found that the results were very similar, so it was decided to present in Figures 6.3 and 6.4 the results for $\dot{m}_f = 0.50$ SLPM.

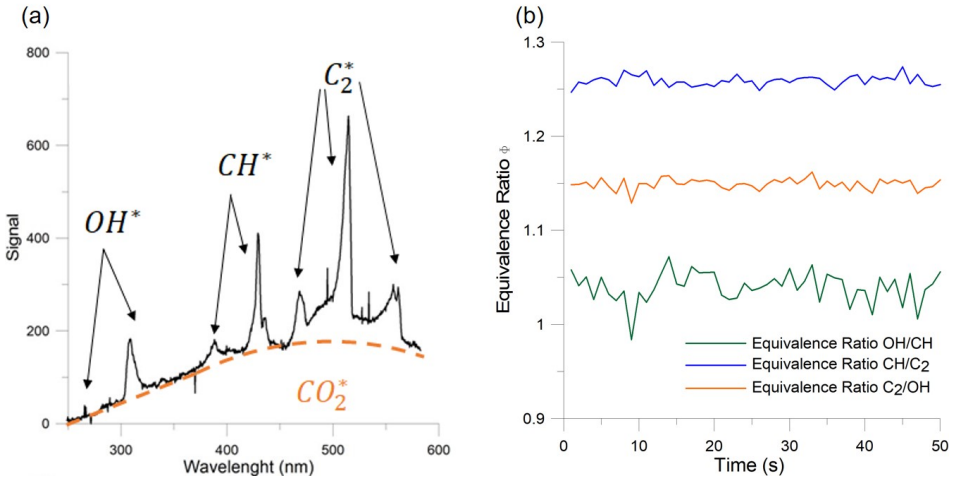

Figure 6.3: (a) Spectrum for tube 1 with the probe in position A (with a slit=0.50 mm) and (b) graph for the equivalence ratio.

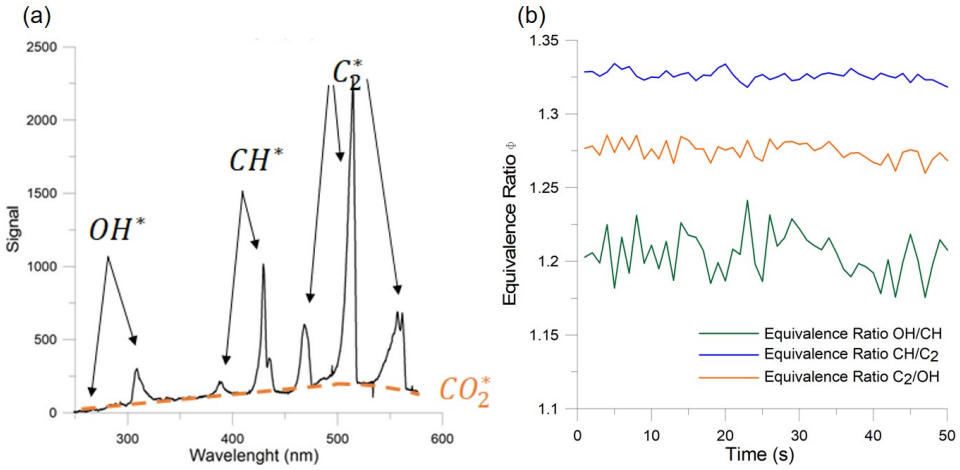

Figure 6.4: (a) Spectrum for tube 1 with the probe in position B (with a slit=0.50 mm) and (b) graph for the equivalence ratio.

In tube 6, for position A, the procedure was the same described for tube 1; for position B, a slit was considered in an attempt to restrict the capture of the optical probe to the zone of interest in the flame. Slits of 0.5 and 0.75 mm were tested. Figure 6.5 shows the results in position A without slit and Figure 6.6 shows the results with a slit of 0.5 mm in position B.

For both tubes, it is possible to see that probe position A it is not good to perform this analysis, due to the great contribution of CO_2^* broadband background radiation. For the probe position B, the flame emission spectra is better, but it is not possible to draw conclusions about equivalence ratio, as it is possible to see in Figures 6.4 and Figure 6.6.

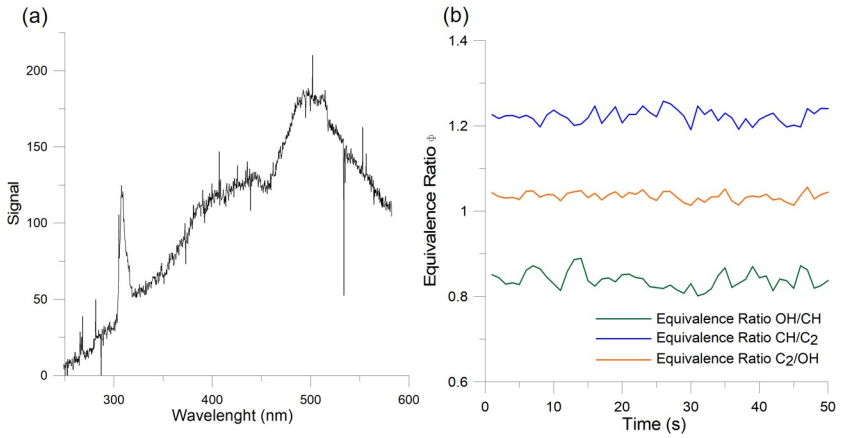

Figure 6.5: (a) Spectrum for tube 6 with the probe in position A (with a slit=0.50 mm) and (b) graph for the equivalence ratio.

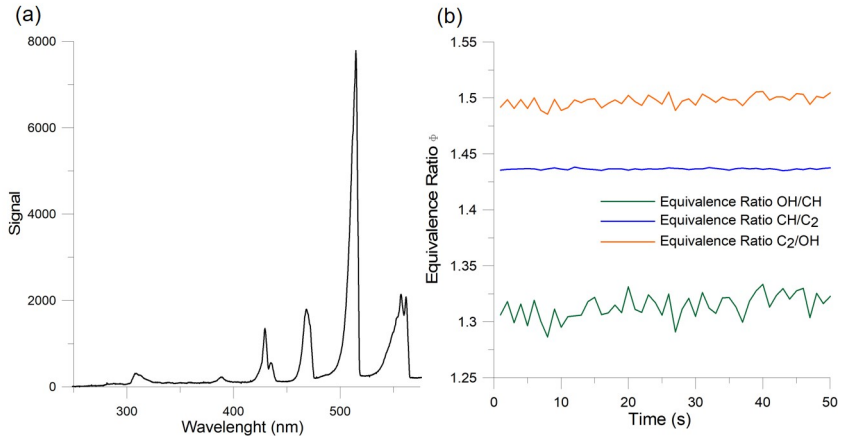

Figure 6.6: (a) Spectrum for tube 6 with the probe in position B (with a slit=0.50 mm) and (b) graph for the equivalence ratio.

6.2.2 Spectroscopy II

After performing the first test, it was concluded that the results of tube 1 were not conclusive enough, so it was decided not to perform further tests with tube 1, focusing only on tube 6 for the next tests.

Focusing on the flame from tube 6, it was decided to deepen the chemiluminescence study in this flame. For that purpose, four different probe positions were considered, three of them in the plume and the other one in the base of the flame. For each position, three different slits (0.20, 0.25, 0.50 mm) were used to see if the results obtained were different. The data collection

time remained at 50 s.

In Figure 6.7 it is possible do observe this four positions numbered from 1 to 4.

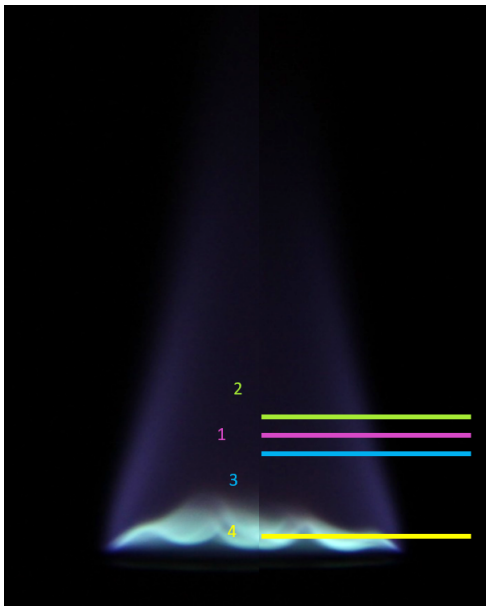

Figure 6.7: Optical probe at position (a) 1, (b) 2, (c) 3 and (d) 4.

The results showed that there were no differences when using different slits at each probe position, proving that there were no influence of the slits on the results. For that reason, the Figures 6.8, 6.9, 6.10 and 6.11 only present results for the slit=0.5 mm.

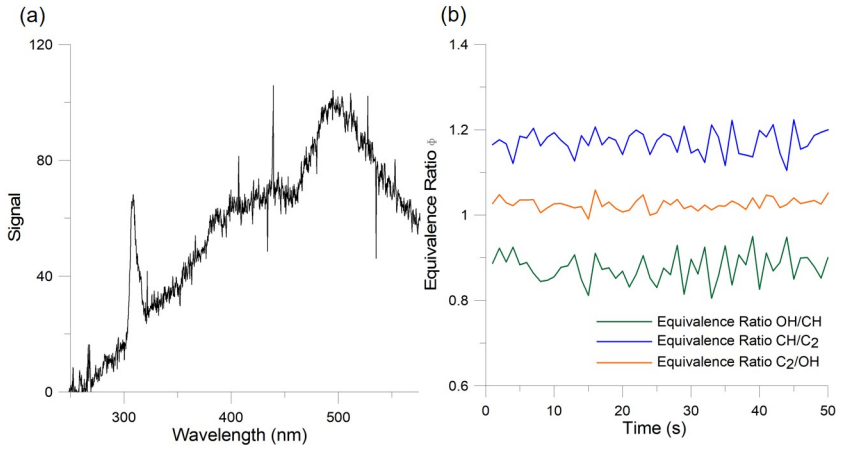

Figure 6.8: (a) Spectrum for tube 6 with the probe in position 1 (with a slit=0.50 mm) and (b) graph for the equivalence ratio.

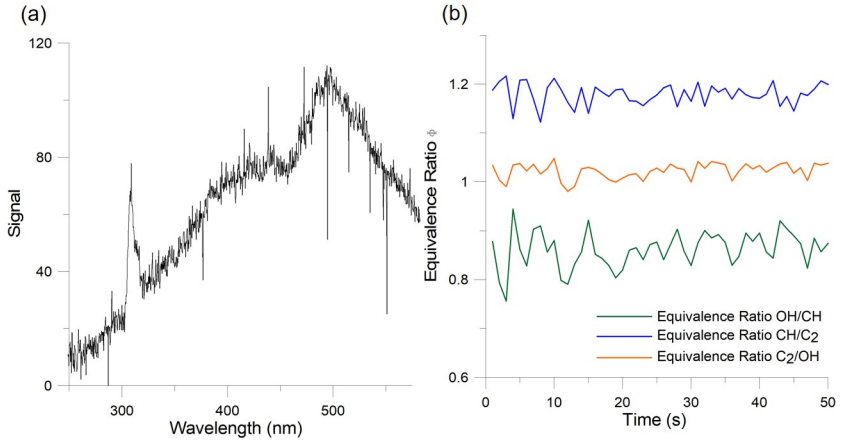

Figure 6.9: (a) Spectrum for tube 6 with the probe in position 2 (with a slit=0.50 mm) and (b) graph for the equivalence ratio.

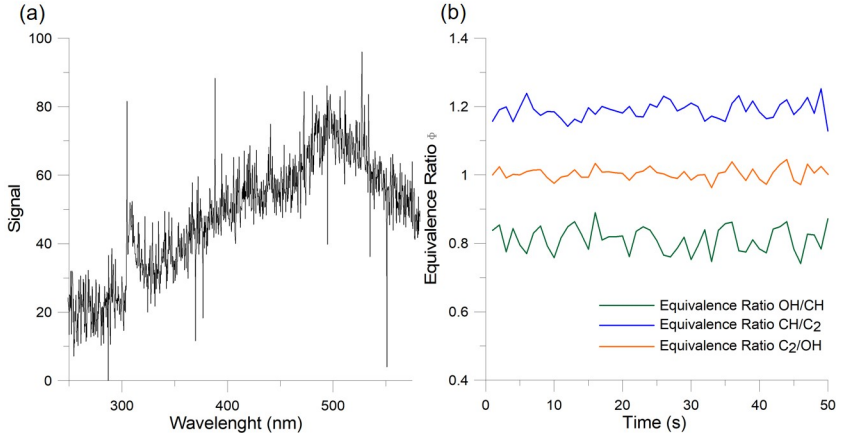

Figure 6.10: (a) Spectrum for tube 6 with the probe in position 3 (with a slit=0.50 mm) and (b) graph for the equivalence ratio.

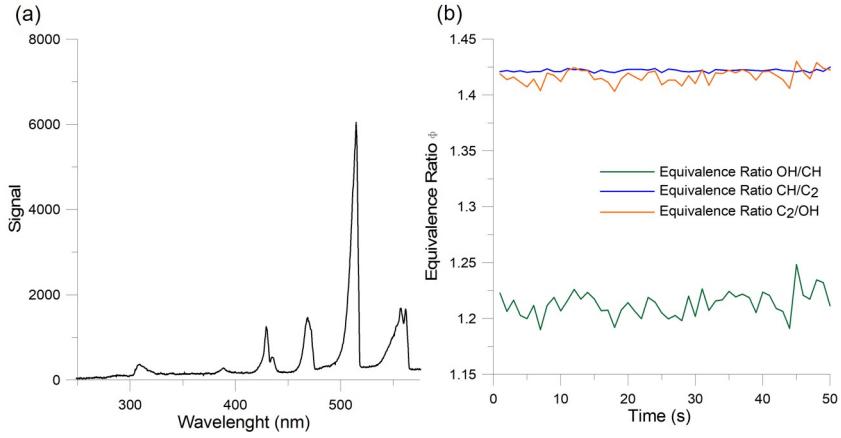

Figure 6.11: (a) Spectrum for tube 6 with the probe in position 4 (with a slit=0.50 mm) and (b) graph for the equivalence ratio.

As it is possible to see in Figures 6.8, 6.9 and 6.10, in fact, probe positions 1, 2 and 3 are

not the best to perform this analysis, with a great contribution of CO_2^* broadband background radiation and, consequently, no conclusions for the equivalence ratio. The same does not occur for probe position 4, presenting conclusive results for the equivalence ratio, only considering CH^*/C_2^* and C_2^*/OH^* ratios. This is because the OH^*/CH^* ratio is characteristic of lean flames and the flame resulting from these tests is rich.

6.2.3 Spectroscopy III

In this last test, the spectroscopy analysis was performed only at tube 6 and the data collection time was increased to 300 s, in order to obtain a better estimate for the equivalence ratio. The only probe position considered was the position 4, which allowed to achieve a more reliable estimate of the equivalence ratio in previous tests.

This test was performed three times to ensure data repeatability and the results verified were the same.

To calculate the value of the equivalence ratio through the ratios, it was necessary to use calibration curves. A reference flame from a Bunsen burner with propane-air mixture were considered and a calibration equation was obtained for each equivalence ratio.

$$OH^*/CH^* \ (r^2 = 0.9647):$$
$$\phi = 0.7976x^{-0.348}$$
$$CH^*/C_2^* \ (r^2 = 0.9970):$$
$$\phi = 0.0855x^2 - 0.4637x + 1.5143$$
$$C_2^*/OH^* \ (r^2 = 0.9992):$$
$$\phi = 0.9715x^{0.1358}$$

The average value for the equivalence ratio ($\phi = 1.44$) was estimated with CH^*/C_2^* and C_2^*/OH^* ratios and it will be useful in the model for the calculation of primary air entrained and could be concluded from Figure 6.12. Figure 6.13 depict the final spectra obtained for this case.

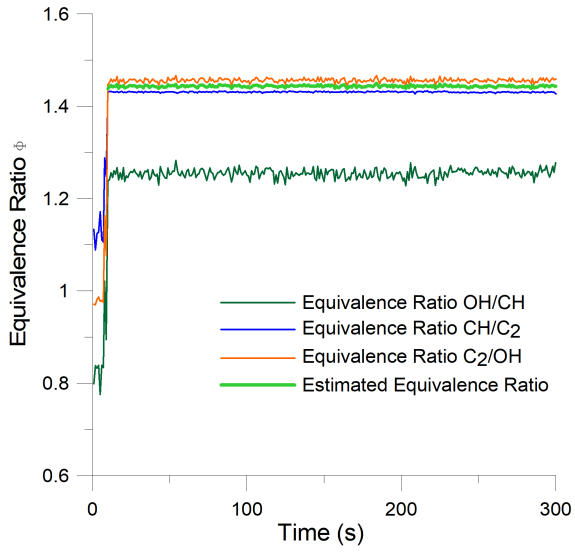

Figure 6.12: Estimated equivalence ratio for the tube 6.

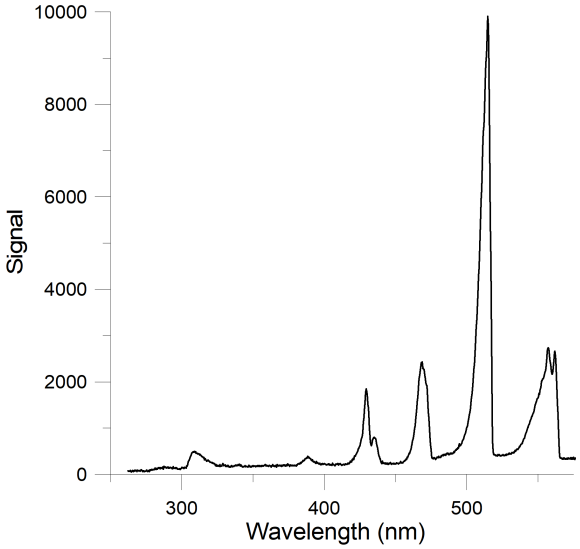

Figure 6.13: Spectrum for tube 6 at position 4.

6.3 Thermography analysis

The main goal of this analysis was to find the temperatures verified at the tube entrance (1) and at the end (2), where the flame was anchored, allowing the input of these values into the mathematical model.

As explained in section 5.3, temperatures were recorded using an infrared camera and the data recorded and processed with the camera software.

In Figure 6.14 it is possible to observe the temperature variation over 300 s, and the temperatures registered was, approximately, 125 °C at the end of the tube (2) and 77 °C at the tube entrance (1).

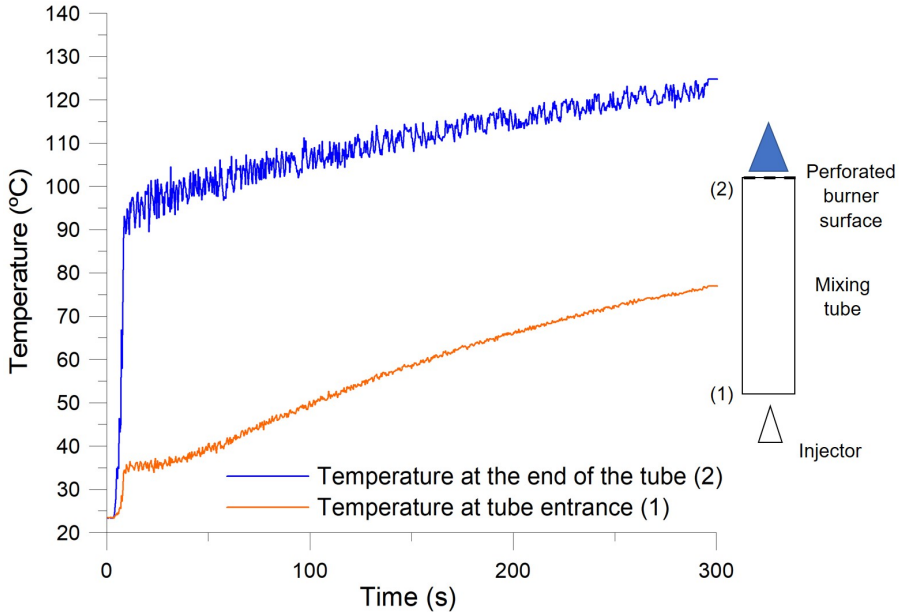

Figure 6.14: Thermography results for a period of 300 s.

These values for tube temperature will be useful for the calculation of primary air entrained, as an input of the mathematical model.

6.4 Mathematical Model

Due to the approximations made in the development of the mathematical model, it was decided to follow a qualitative approach in the analysis of the results.

As the objective was to reach a value for the primary air entrained, after deriving Equation 4.11, an algorithm was developed in Mat Lab to solve it, in order to discover this unknown. All other variables were known and then these inputs introduced in the algorithm.

With this mathematical model it was possible to study the relations between the different variables considered. Changing the diameter and keeping the tube temperature, there is a variation of entrained air with variation of the tube diameter, as can be seen in Figure 6.15. Primary entrained air increases with increasing diameter, contrary to what happens with the equivalence ratio, that decreases. In same conditions, changing the headloss coefficient k_{12}, there is a variation of entrained air with tube diameter, for each coefficient, where, for the same diameter, increasing k_{12}, there is a decreasing in primary entrained air.

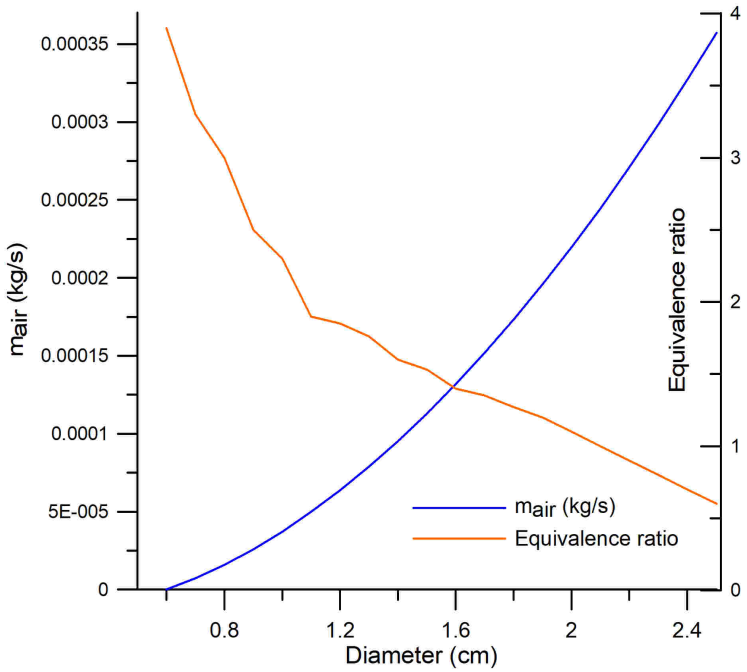

Figure 6.15: Relation between primary entrained air and equivalence ratio with tube diameter.

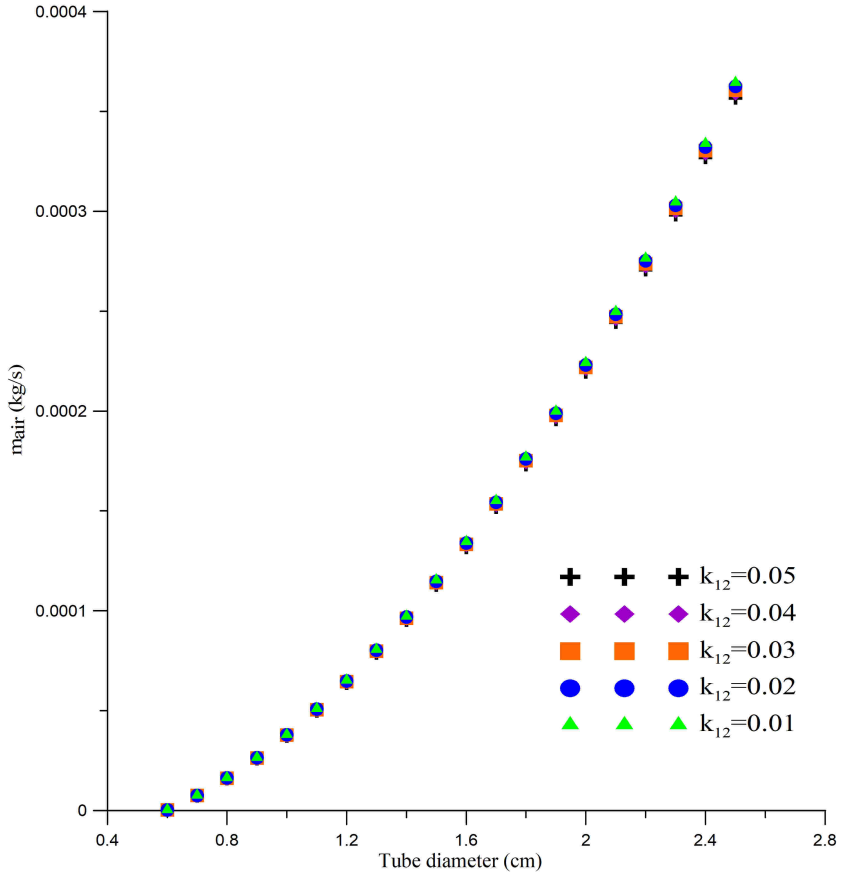

Figure 6.16: Relation between primary entrained air and tube diameter for different headloss coefficient (k_{12}).

Chapter 7

Conclusions

With the main objective of understand how the emissions of pollutants can be reduced in gas water heaters, the work was divided into three phases, where a study of the materials to be used in open flue burners was made in a first approach. Two different analysis were made on brass, copper, stainless steel, alumina and silicon carbide, using Cambridge Engineering Software and Simapro, to accomplish which of these materials might be the best to use for the intended purpose. It has been concluded from here that it can be difficult to combine all the important characteristics into only one material with reduced impact in environment, given that, according to CES analysis, the material to use would be silicon carbide, and according to LCA analysis would be alumina.

As a second approach, experimental tests were performed with different materials and geometries. It was very important to know what kind of flames resulted from different geometries and materials used in burners, due to the impossibility of carrying out stability tests. Two tubes were chosen to make the spectroscopy tests and the results were more conclusive for the tube with larger diameter, using slits and in a position as close as possible to the burner surface zone. With spectroscopy analysis and with a reference flame from a Bunsen burner with propane-air mixture, a calibration equation was obtained for each ratio, allowing estimating the equivalence ratio, which was found to be above 1, being the flame rich. From the thermography analysis, temperatures were obtained from both ends of the tube.

The final approach was to bring experimental results altogether to complement the mathematical model that allows to predict the quantity of primary entrained air into the burner. Since the temperatures of the two extremities of the tube increase in the same way, the equivalence ra-

tio remains approximately constant during the same period of time and a rich regime occurred, it was believed that the entrained air does not change with increasing temperature and buoyancy has a greater influence, overlapping to the effect of the heat transferred through the material. There is a limitation of this model for the different materials considered and it was not possible to input this data in the model.

7.1 Future Work

As future work, some improvements can be made both in the experimental part and in mathematical model.

In the experimental part, a different setup could be set up where, in addition to the gas flow, it is possible to quantify the air flow using laser techniques, in order to easily obtain a value for the equivalence ratio.

Regarding the mathematical model, there is a limitation and it is not possible to introduce data regarding the material considered, so some improvements must be made to the model to overcome this problem.

One suggestion may be to develop another mathematical model for the heat transferred along the tube in a way to really understand the effect of the temperature on the heat transfer in the tube.

Another suggestion may be to deepen the study on tubes geometry (length and thickness) to understand what impact it may have on the primary air entrained and, consequently, on pollutant emissions.

Bibliography

[1] A Namkhat and S Jugjai. Primary air entrainment characteristics for a self-aspirating burner: Model and experiments. *Energy*, 35(4):1701–1708, 2010.

[2] Mário Costa and Pedro Coelho. *Combustão*. Orion, 2012.

[3] Shuhn-Shyurng Hou, Chien-Ying Lee, and Ta-Hui Lin. Efficiency and emissions of a new domestic gas burner with a swirling flame. *Energy Conversion and Management*, 48(5): 1401–1410, 2007.

[4] Sumrerng Jugjai and Natthawut Rungsimuntuchart. High efficiency heat-recirculating domestic gas burners. *Experimental thermal and fluid science*, 26(5):581–592, 2002.

[5] HS Zhen, J Miao, CW Leung, CS Cheung, and ZH Huang. A study on the effects of air preheat on the combustion and heat transfer characteristics of bunsen flames. *Fuel*, 184: 50–58, 2016.

[6] James R Maughan, James R Cahoe, and Reza Ghassemzadeh. Autoregulation of primary aeration for atmospheric burners, April 14 1992. US Patent 5,104,311.

[7] David G. Goodwin, Harry K. Moffat, and Raymond L. Speth. Cantera: An object- oriented software toolkit for chemical kinetics, thermodynamics, and transport processes. `http://www.cantera.org`, 2017. Version 2.3.0.

[8] Gregory P. Smith, David M. Golden, Michael Frenklach, Nigel W. Moriarty, Boris Eitenee, Mikhail Goldenberg, C. Thomas Bowman, Ronald K. Hanson, Soonho Song, William C. Gardiner Jr., Vitali V. Lissianski, and Zhiwei Qin. Gri3.0 mechanism, 1999. URL `http://www.me.berkeley.edu/gri_mech/`.

[9] Sean D Salusbury and Jeffrey M Bergthorson. Maximum stretched flame speeds of laminar

premixed counter-flow flames at variable lewis number. *Combustion and Flame*, 162(9): 3324–3332, 2015.

[10] University of Wisconsin-Madison College of Engineering. Me349 engineering design projects - introduction to materials selection. URL http://homepages.cae.wisc.edu/~me349/lecture_notes/material_selection.pdf. Accessed in 2-1-2017.

[11] Michael F Ashby. *Materials and the environment: eco-informed material choice*. Elsevier, 2012.

[12] Wikipedia. Stainless steel. URL https://en.wikipedia.org/wiki/Stainless_steel. Accessed in 2-1-2017.

[13] Azo Materials. Stainless steels - specifications, grades and properties, supplier data by aalco, . URL https://www.azom.com/article.aspx?ArticleID=2874#_Specifications. Accessed in 2-1-2017.

[14] Azo Materials. Metal alloys - properties and applications of brass and brass alloys by austral wright metals, . URL https://www.azom.com/article.aspx?ArticleID=4387. Accessed in 18-8-2017.

[15] Granta Material Intelligence. Ces selector 2010, . URL http://www.grantadesign.com/products/ces/whatsnew10.htm. Accessed in 18-12-2016.

[16] Terence Bell. The uses and properties of bronze. The balance. URL https://www.thebalance.com/metal-profile-brass-2340129. Accessed in 18-8-2017.

[17] M Li and SJ Zinkle. 4.20 physical and mechanical properties of copper and copper alloys. *Comprehensive Nuclear Materials*, pages 667–690, 2012.

[18] Elemental Matter. Copper properties. URL http://www.elementalmatter.info/copper-properties.htm. Accessed in 18-12-2016.

[19] ThoughtCo. Copper facts: Chemical and physical properties. URL https://www.thoughtco.com/copper-facts-chemical-and-physical-properties-606521. Accessed in 18-12-2016.

[20] Azo Materials. Aluminium - specifications, properties, classifications and classes, supplier data by aalco, . URL https://www.azom.com/article.aspx?ArticleID=2863. Accessed in 8-9-2017.

[21] Aluminium design. Properties of aluminium. URL http://www.aluminiumdesign.net/why-aluminium/properties-of-aluminium/. Accessed in 8-9-2017.

[22] Accuratus. Aluminum oxide, al2o3 ceramic properties, . URL http://accuratus.com/alumox.html. Accessed in 18-12-2016.

[23] M Abdul Mujeebu, M Zulkifly Abdullah, MZ Abu Bakar, AA Mohamad, RMN Muhad, and MK Abdullah. Combustion in porous media and its applications–a comprehensive survey. *Journal of environmental management*, 90(8):2287–2312, 2009.

[24] Accuratus. Silicon carbide, sic ceramic properties, . URL http://accuratus.com/silicar.html. Accessed in 18-12-2016.

[25] Granta Material Intelligence, . URL http://www.grantadesign.com/. Accessed in 18-12-2016.

[26] The global development research center. Defining life cycle assessment. URL https://www.gdrc.org/uem/lca/lca-define.html. Accessed in 18-12-2016.

[27] María D Bovea, Elena Díaz-Albo, Antonio Gallardo, Francisco J Colomer, and Julio Serrano. Environmental performance of ceramic tiles: improvement proposals. *Materials & Design*, 31(1):35–41, 2010.

[28] Ellen MacArthur Foundation. Circular economy overview. URL https://www.ellenmacarthurfoundation.org/circular-economy/overview/concept. Accessed in 18-10-2017.

[29] *Environmental management – Life cycle assessment – Principles and framework*. American National Standards Institute, 1 edition, July 1997.

[30] Elizabeth Lynn Belcastro. Life cycle analysis of a ceramic three-way catalytic converter. Master's thesis, Virginia Polytechnic Institute, 2012.

[31] MJ Goedkoop, R Heijungs, M Huijbregts, A De Schryver, JVZR Struijs, R Van Zelm, et al. A life cycle impact assessment method which comprises harmonised category indicators at the midpoint and the endpoint level. report i: Characterisation. *Den Haag*, 2009.

[32] SimaPro. About simparo. URL `https://simapro.com/about/`. Accessed in 18-12-2016.

[33] PRé Putting the metrics into sustainability. Normalisation: New developments in normalisation sets. URL `https://www.pre-sustainability.com/news/the-normalisation-step-in-lcia`. Accessed in 2-1-2017.

[34] Christos Keramiotis, Björn Stelzner, Dimosthenis Trimis, and Maria Founti. Porous burners for low emission combustion: An experimental investigation. *Energy*, 45(1):213–219, 2012.

[35] Yunus A Cengel, Robert H Turner, John M Cimbala, and Mehmet Kanoglu. *Fundamentals of thermal-fluid sciences*. McGraw-Hill New York, NY, 2008.

Appendix A

Experimental results - Morphological analysis

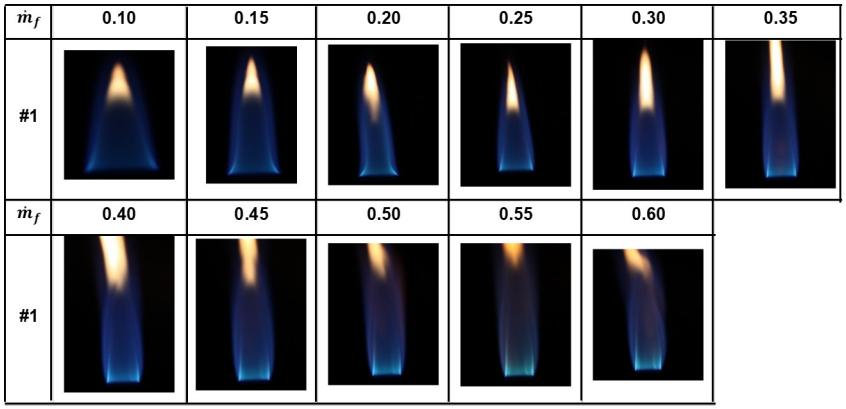

Figure A.1: Flames obtained for tube 1 with a gas flow rate from 0.10 to 0.60 SLPM.

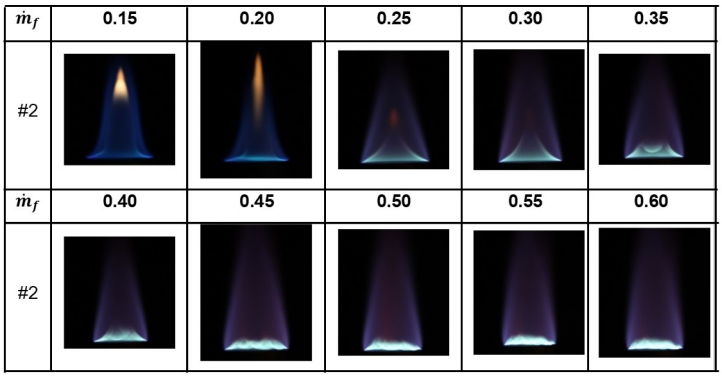

Figure A.2: Flames obtained for tube 2 with a gas flow rate from 0.15 to 0.60 SLPM.

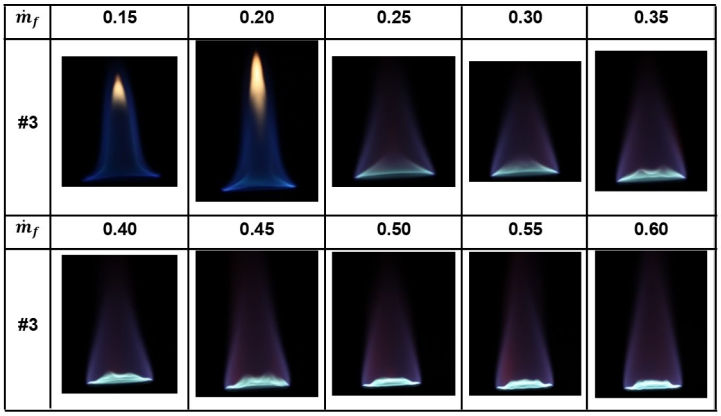

Figure A.3: Flames obtained for tube 3 with a gas flow rate from 0.15 to 0.60 SLPM.

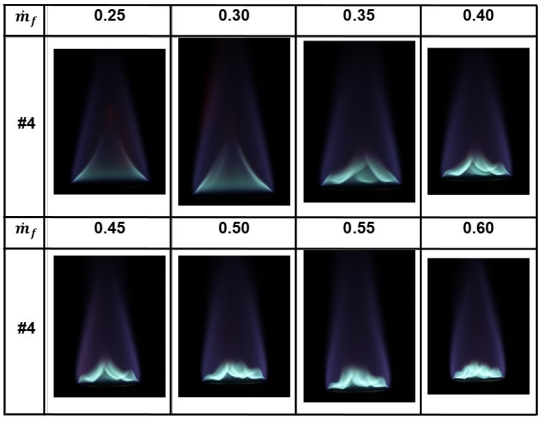

Figure A.4: Flames obtained for tube 4 with a gas flow rate from 0.25 to 0.60 SLPM.

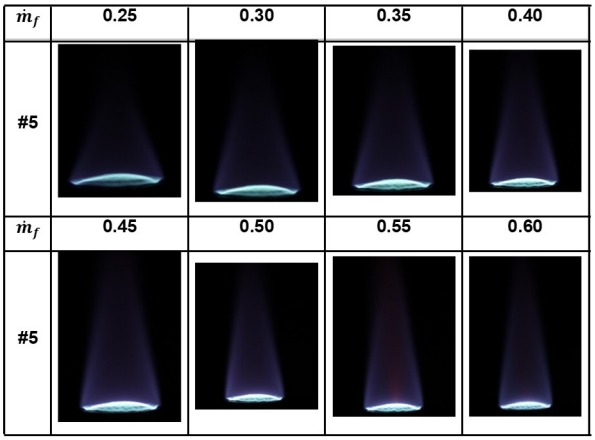

Figure A.5: Flames obtained for tube 5 with a gas flow rate from 0.25 to 0.60 SLPM.

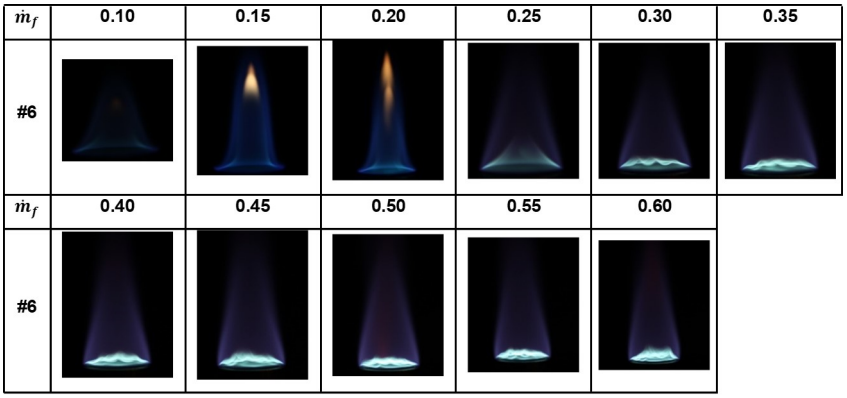

Figure A.6: Flames obtained for tube 6 with a gas flow rate from 0.10 to 0.60 SLPM.

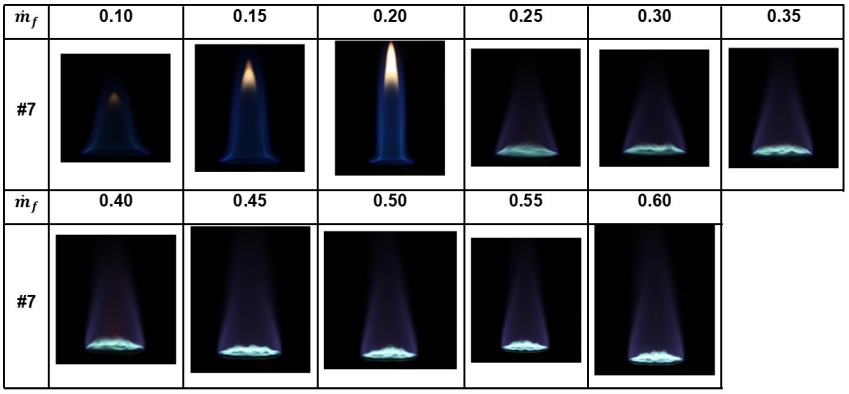

Figure A.7: Flames obtained for tube 7 with a gas flow rate from 0.10 to 0.60 SLPM.

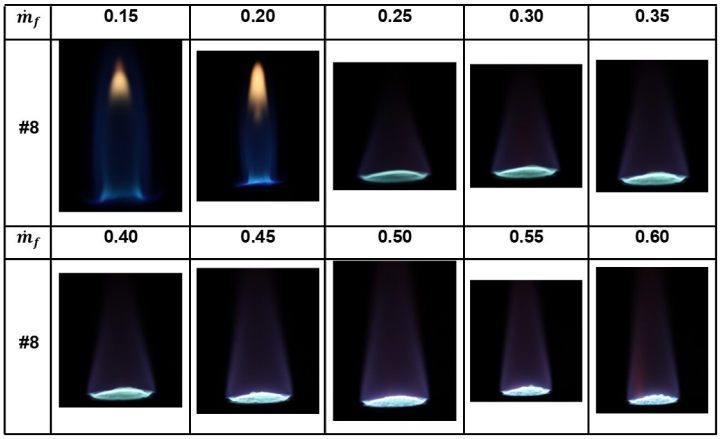

Figure A.8: Flames obtained for tube 8 with a gas flow rate from 0.15 to 0.60 SLPM.

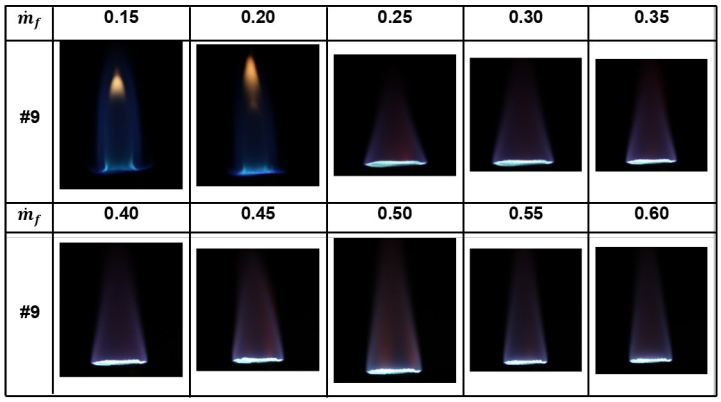

Figure A.9: Flames obtained for tube 9 with a gas flow rate from 0.15 to 0.60 SLPM.

Appendix B

Life Cycle Assessment results

In this appendix the flow diagram that define the inputs and outputs in the system are presented.

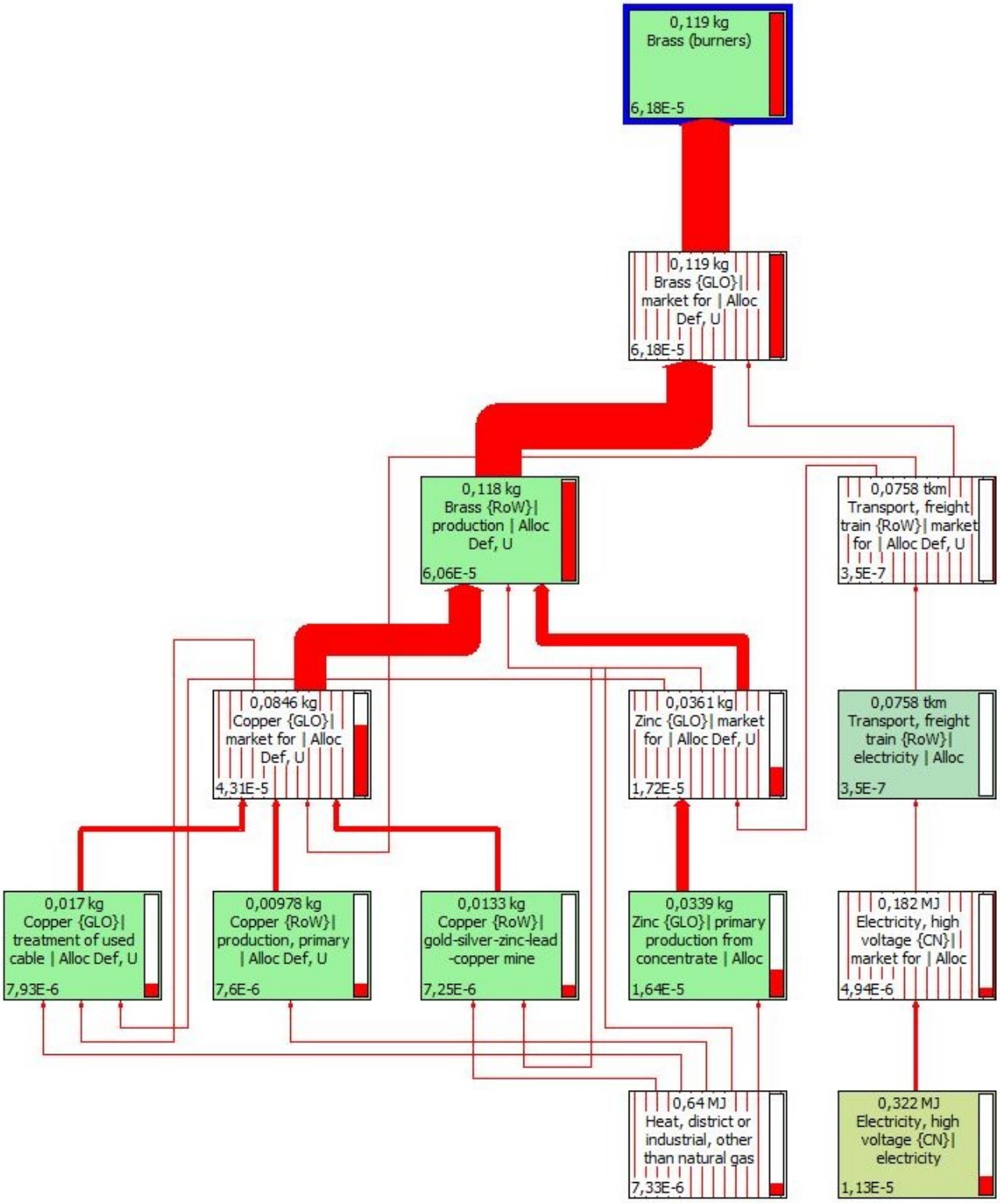

Figure B.1: Flow diagram for 0.119 kg of brass. Cut-off=10.9%.

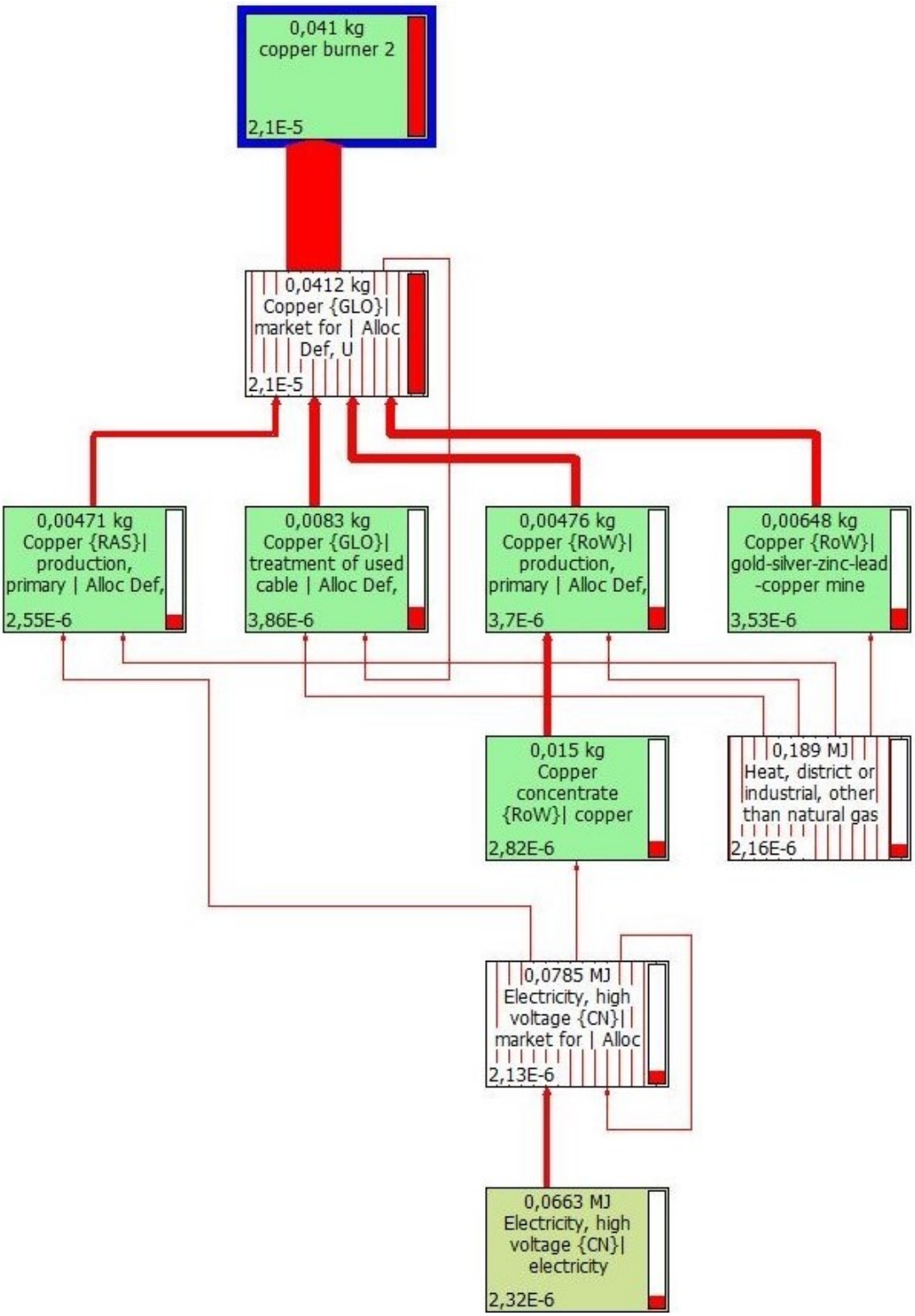

Figure B.2: Flow diagram for 0.041 kg of copper. Cut-off=10%.

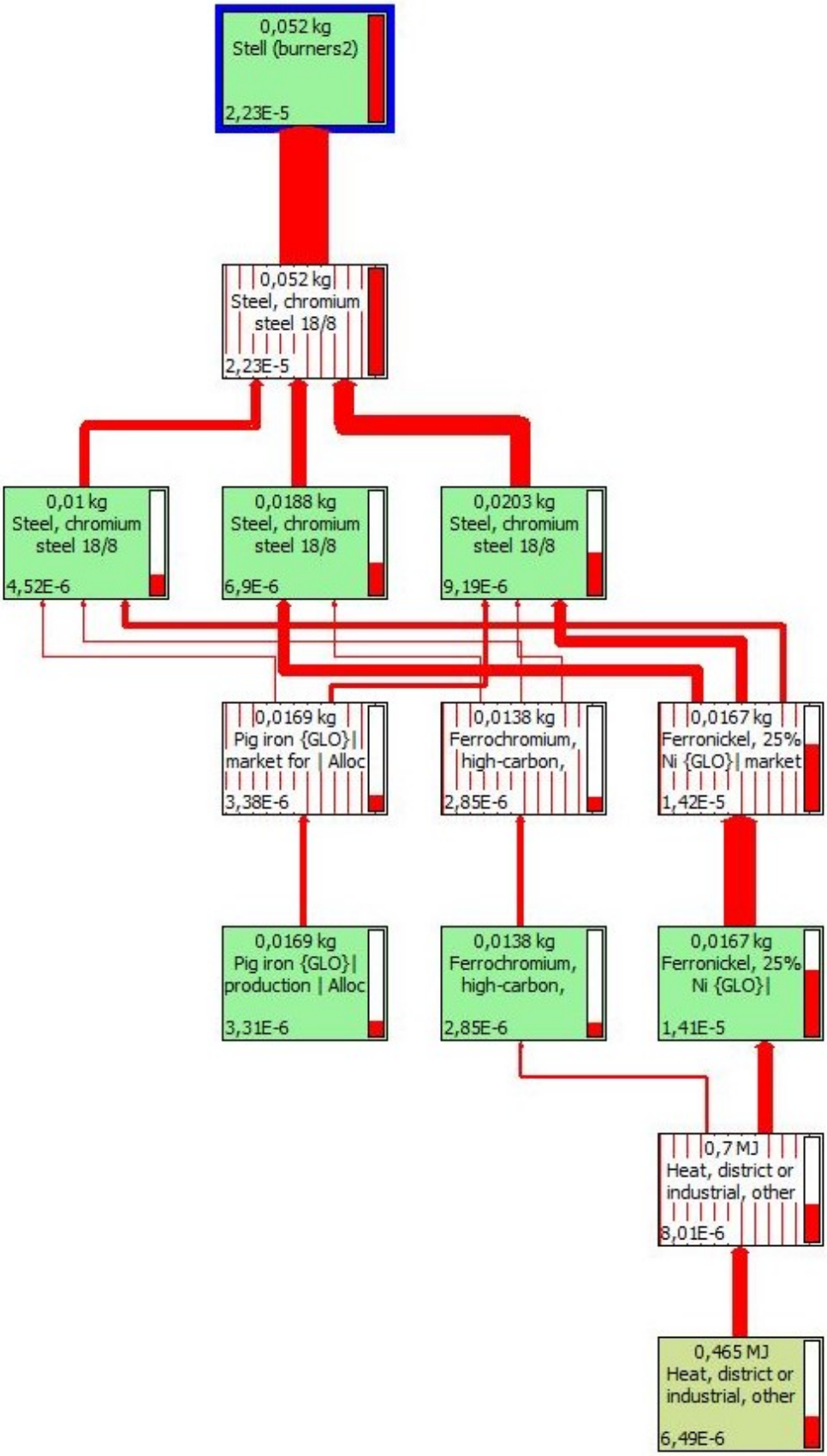

Figure B.3: Flow diagram for 0.052 kg of stainless steel. Cut-off=10%.

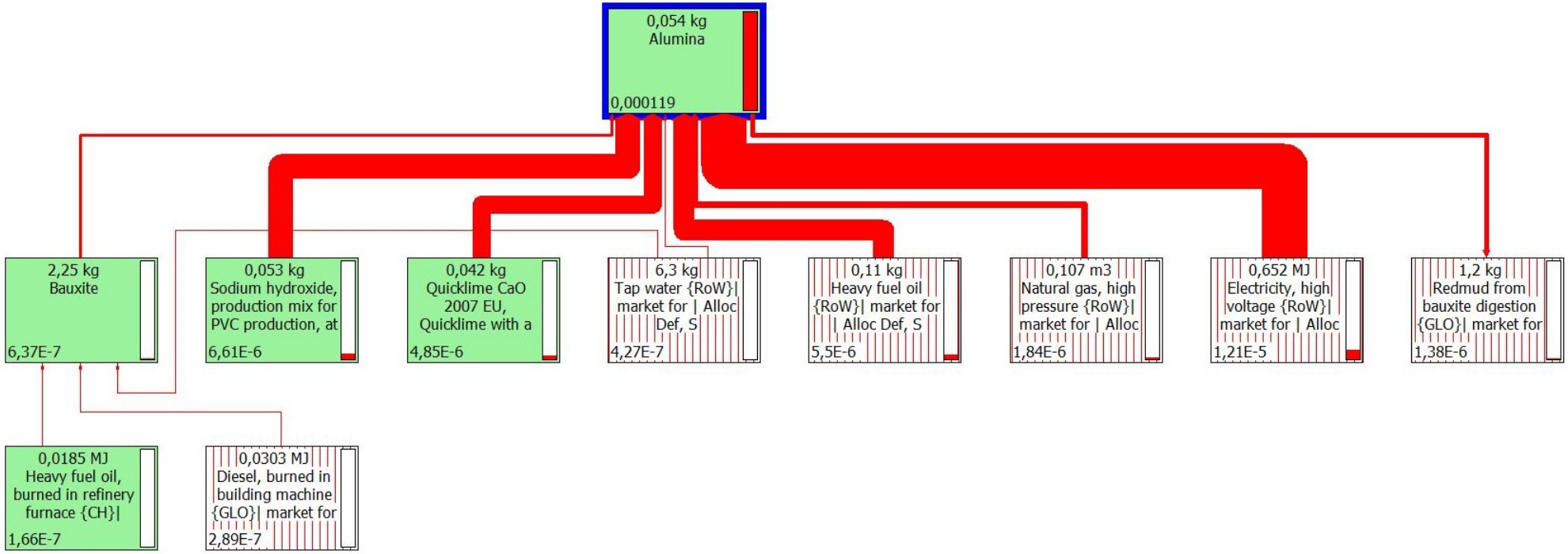

Figure B.4: Flow diagram for 1.19E-04 kg of alumina. Cut-off=0.1%.

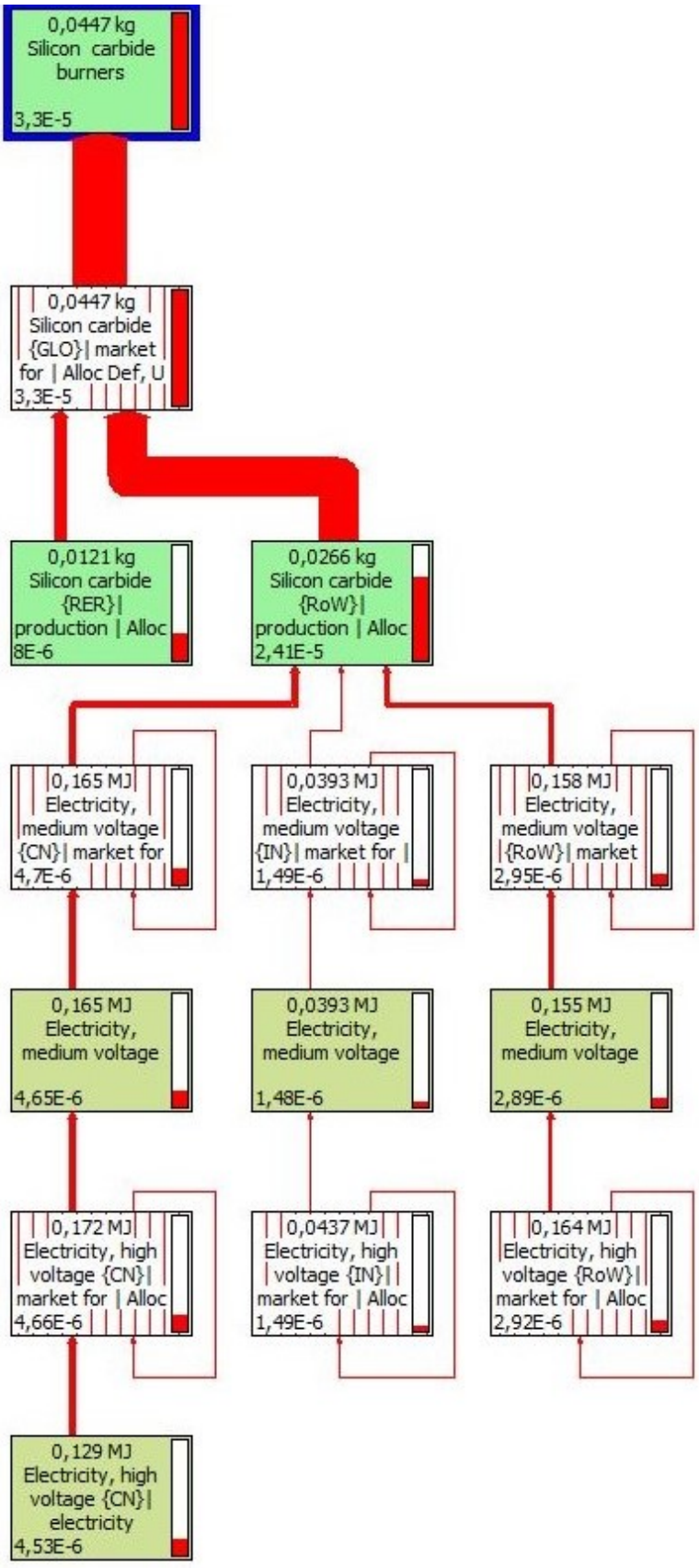

Figure B.5: Flow diagram for 0.0447 kg of silicon carbide. Cut-off=4%.